

## Article

# Bimetallic Pt-IrO<sub>x</sub>/g-C<sub>3</sub>N<sub>4</sub> Photocatalysts for the Highly Efficient Overall Water Splitting under Visible Light

Nikolay D. Sidorenko <sup>1</sup>, Polina A. Topchiyan <sup>2</sup>, Andrey A. Saraev <sup>1</sup>, Evgeny Yu. Gerasimov <sup>1</sup>,  
Angelina V. Zhurenok <sup>1</sup>, Danila B. Vasilchenko <sup>2</sup> and Ekaterina A. Kozlova <sup>1,\*</sup>

<sup>1</sup> Federal Research Center Boreskov Institute of Catalysis, 630090 Novosibirsk, Russia; gerasimov@catalysis.ru (E.Y.G.); angelinazhurenok@gmail.com (A.V.Z.)

<sup>2</sup> Nikolaev Institute of Inorganic Chemistry, Siberian Branch of the Russian Academy of Science, 630090 Novosibirsk, Russia; vasilchenko@niic.nsc.ru (D.B.V.)

\* Correspondence: kozlova@catalysis.ru

**Abstract:** Two series of bimetallic photocatalysts (0.5% Pt/0.01–0.5% IrO<sub>x</sub>/g-C<sub>3</sub>N<sub>4</sub> and 0.1% Pt/0.01–0.1% IrO<sub>x</sub>/g-C<sub>3</sub>N<sub>4</sub>) were synthesized by the thermolysis of melamine cyanurate and a successive deposition of platinum and iridium labile complexes (Me<sub>4</sub>N)<sub>2</sub>[Pt<sub>2</sub>(μ-OH)<sub>2</sub>(NO<sub>3</sub>)<sub>8</sub>] and *fac*-[Ir(H<sub>2</sub>O)<sub>3</sub>(NO<sub>2</sub>)<sub>3</sub>]. The synthesized photocatalysts were studied by a set of physicochemical analysis techniques. Platinum exists in two states, with up to 60% in metallic form and the rest in the Pt<sup>2+</sup> state, while iridium is primarily oxidized to the Ir<sup>3+</sup> state, which was determined by X-ray photoelectron spectroscopy (XPS). The specific surface area (S<sub>BET</sub>), which is determined by low-temperature nitrogen adsorption, ranges from 80 to 100 m<sup>2</sup> g<sup>-1</sup> and the band gap energy (E<sub>g</sub>) value is in the range of 2.75–2.80 eV as found by diffuse reflectance spectroscopy (DRS). The activity of the photocatalysts was tested in the photocatalytic production of hydrogen from ultrapure water under visible light (λ = 400 nm). It was found that the splitting of water occurs with the formation of the stoichiometric amount of H<sub>2</sub>O<sub>2</sub> as an oxidation product. Two photocatalysts 0.5% Pt/0.01% IrO<sub>x</sub>/g-C<sub>3</sub>N<sub>4</sub> and 0.1% Pt/0.01% IrO<sub>x</sub>/g-C<sub>3</sub>N<sub>4</sub> showed the highest activity at 100 μmol h<sup>-1</sup> g<sub>cat</sub><sup>-1</sup>, which is among the highest in H<sub>2</sub> production published for such systems.

**Keywords:** g-C<sub>3</sub>N<sub>4</sub>; photocatalytic water splitting; hydrogen peroxide; visible light



**Citation:** Sidorenko, N.D.; Topchiyan, P.A.; Saraev, A.A.; Gerasimov, E.Y.; Zhurenok, A.V.; Vasilchenko, D.B.; Kozlova, E.A. Bimetallic Pt-IrO<sub>x</sub>/g-C<sub>3</sub>N<sub>4</sub> Photocatalysts for the Highly Efficient Overall Water Splitting under Visible Light. *Catalysts* **2024**, *14*, 225. <https://doi.org/10.3390/catal14040225>

Academic Editors: Narendra Kumar, Leonarda Liotta and Konstantin Ivanov Hadjiivanov

Received: 26 February 2024

Revised: 24 March 2024

Accepted: 26 March 2024

Published: 28 March 2024



**Copyright:** © 2024 by the authors. Licensee MDPI, Basel, Switzerland. This article is an open access article distributed under the terms and conditions of the Creative Commons Attribution (CC BY) license (<https://creativecommons.org/licenses/by/4.0/>).

## 1. Introduction

The transition to a carbon-free and low-carbon economy is now being seriously considered, and therefore there is a huge interest in hydrogen as an ideal energy carrier [1,2]. Photocatalytic water splitting with hydrogen production is widely regarded as the most promising strategy for the conversion of solar energy into chemical energy [3–7].

Unfortunately, the quantum efficiency of this process is usually low due to the back reaction between the evolved hydrogen and oxygen and the recombination of electron–hole pairs [8]. Therefore, most investigations are devoted to photocatalytic hydrogen production not by water splitting, but by its reduction through the use of available organic and inorganic electron donors in aqueous solutions [9]. The addition of so-called “sacrificial agents” reduces the recombination of electron–hole pairs and thus increases the quantum efficiency of hydrogen production [10]. The maximum rate of hydrogen production in systems with electron donors is several orders of magnitude higher than the rate of hydrogen production during water splitting [11]. However, the use of “sacrificial agents” has a fundamental disadvantage—the need for the constant introduction of an electron donor into the system. Moreover, it is necessary to select a photocatalyst that is active in the presence of a specific “sacrificial agent”. Therefore, recent research has tended to move from systems containing electron donors to photocatalytic splitting of pure water [12–15].

For the complete water splitting under normal conditions, the standard Gibbs free energy is very high and amounts to  $\Delta_r G^\circ_{298} = +237.2 \text{ kJ}\cdot\text{mol}^{-1}$ . In addition, the oxidation

of water usually requires a much higher overvoltage than the reduction in protons [9]. It is known that the four-electron oxidation of water is a complex process that occurs with great kinetic constraints [16]. In addition, when obtaining a mixture of hydrogen and oxygen, safety issues arise, and efforts must be made to separate the components of the mixture [17].

Photocatalytic water splitting is known to follow two different mechanisms: a thermodynamically favored ( $E = 1.23$  eV vs. NHE) four-electron pathway [18]:



and a kinetically favored ( $E = 1.78$  eV vs. NHE) two-electron pathway:



It is believed that under ambient conditions, process (2) is more probable [16]. Note that this process is also considered favorable because hydrogen peroxide is a valuable product itself [18–20].

The most frequently studied photocatalysts for water splitting are graphene-based structures [15,21–23] and polymeric graphite-like carbon nitride  $g\text{-C}_3\text{N}_4$  [18,19,24]. Unlike photocatalysts based on transition metal sulfides,  $g\text{-C}_3\text{N}_4$  is an environmentally friendly material.  $g\text{-C}_3\text{N}_4$  is a semiconductor with a band gap of 2.7 eV ( $\lambda = 460$  nm) and with valence band levels at +1.6 V vs. NHE and the conduction band at  $-1.1$  V vs. NHE [25,26]. The latter is one of the most negative values for known semiconductor photocatalysts, which favors photocatalytic reduction. In addition,  $g\text{-C}_3\text{N}_4$  is able to catalyze the two-electron process of formation of  $\text{H}_2\text{O}_2$  [27,28]. Graphitic carbon nitride is usually obtained by thermal polycondensation of inexpensive nitrogen-containing precursors, such as cyanamide and dicyandiamide, melamine, urea, and thiourea [29]. However, the resulting  $g\text{-C}_3\text{N}_4$  has a small specific surface area. In order to increase the surface area and obtain materials with higher catalytic activity, various methods are proposed. For example, in our group, a new synthetic technique, based on thermolysis of a melamine cyanurate complex, has been proposed for the formation of  $g\text{-C}_3\text{N}_4$  with a high surface area and photocatalytic activity [30–32].

For the splitting of water by reaction (1) and reaction (2), the surface of the photocatalyst must contain additional cocatalysts for the reduction and oxidation of water, respectively [16,33]. Suitable cocatalysts can reduce energy barriers for reduction/oxidation by reducing the activation energy [33]. In order to reduce the energy barriers to reduction/oxidation, appropriate cocatalysts are applied. For example, platinum group metals such as Pt, Rh, Ru, and Ir, as well as Ni, can be used as a cocatalyst for hydrogen evolution [34,35]. Metal oxides such as Co, Fe, Ni, Mn, Ru, and Ir oxides are commonly used as oxygen production cocatalysts [34,36]. For the complete water splitting, systems based on graphitic carbon nitride with cocatalysts such as Pt-CoP/ $g\text{-C}_3\text{N}_4$  [37], Pt-PtO<sub>x</sub>-CoO<sub>x</sub>/ $g\text{-C}_3\text{N}_4$  [38], Rh-RhO<sub>x</sub>/ $g\text{-C}_3\text{N}_4$  [39], Pt-IrO<sub>2</sub>/ $g\text{-C}_3\text{N}_4$  [6], Pt/(K<sup>+</sup>-doped) $g\text{-C}_3\text{N}_4$  [20], or Pt-CoP/ $g\text{-C}_3\text{N}_4$  [8] have been proposed. These systems showed high activity in complete water splitting; however, the content of noble metals used in them was quite high—from 1 to 5 wt.%. The possibility of synthesizing photocatalysts with small amounts of noble metals has not been studied, although the high content of these components leads to a significant increase in the cost of the material.

This research was aimed at the synthesis of  $g\text{-C}_3\text{N}_4$ -based photocatalysts containing platinum and iridium oxide cocatalysts with low content of noble metals (<0.5 wt.%). In our previous works, we have developed novel approaches for the synthesis of active photocatalysts for two processes—hydrogen evolution from aqueous solutions of TEOA and oxygen evolution from aqueous solutions of NaIO<sub>4</sub>. For the first process, 0.01–0.5% Pt/ $g\text{-C}_3\text{N}_4$  photocatalysts were prepared by thermal treatment of melamine–cyanuric acid supramolecular complex and further sorption of platinum nitrate complexes as a precursor of Pt cocatalyst [30]. For the second process, 0.005–0.5% IrO<sub>x</sub>/ $g\text{-C}_3\text{N}_4$  photocatalysts were prepared via deposition of Ir aqua/nitro complex onto the surface of  $g\text{-C}_3\text{N}_4$  with further

thermal treatment in air [32]. It was shown that at high activity in the production of oxygen from an electron acceptor solution,  $\text{NaIO}_4$ , the  $\text{IrO}_x/\text{g-C}_3\text{N}_4$  photocatalysts show very low activity in the production of hydrogen, i.e., they catalyze only the process of oxygen formation [32]. Thus, we assumed that a system  $\text{IrO}_x/\text{Pt}/\text{g-C}_3\text{N}_4$  with two supported cocatalysts (“reductive” Pt and “oxidative”  $\text{IrO}_x$ ) would be active in the complete decomposition of water. The main task was to provide the synthesis of photocatalysts in such a way that platinum would be reduced to the metallic state, while iridium would remain in an oxide state. Based on this idea, we synthesized two series of samples  $\text{IrO}_x/\text{Pt}/\text{g-C}_3\text{N}_4$  with the Pt weight content of 0.5 and 0.1% and the Ir content of 0.01–0.5 wt.%. The catalysts provided photocatalytic splitting of water without the addition of donors or acceptors of electrons under the action of visible light.

Thus, the systematic analysis carried out to understand the mutual influence of platinum and iridium particles in bimetallic  $\text{IrO}_x/\text{Pt}/\text{g-C}_3\text{N}_4$  photocatalysts on the overall activity of such materials in the reaction of water splitting into  $\text{H}_2$  and  $\text{H}_2\text{O}_2$  is the main novelty of this work. By using an original synthetic approach to deposit cocatalysts based on our previous studies of  $\text{Pt}/\text{g-C}_3\text{N}_4$  photocatalyst [30], several different combinations of Ir and Pt states of cocatalysts with different Pt/Ir ratios were realized on  $\text{g-C}_3\text{N}_4$  surface. The activities of the resulting ensembles were analyzed along with the data about their structure revealed by the series of methods.

## 2. Results

### 2.1. Preparation of the Pt-Ir/ $\text{C}_3\text{N}_4$ Photocatalysts

Earlier it was shown that the best cocatalysts for the production of hydrogen and oxygen are platinum in the metallic state and ionic forms of iridium, respectively [29–32]. The objective of this study was to select a combination of cocatalysts that would produce hydrogen from water without the addition of organic substances—electron donors.

Our main synthesis strategy was Method 1. This procedure, with the metal deposition steps separated from each other, leads to an independent distribution of Ir and Pt particles (see below). However, to check the influence of a synthesis method on the structure and activity of catalysts, two modified approaches (Methods 2 and 3) were also tested.

### 2.2. Photocatalyst Characterization

The synthesized photocatalysts were characterized by XRD. It was proved that all three synthesis methods provide the formation of graphite-like carbon nitride  $\text{g-C}_3\text{N}_4$ : in the X-ray patterns, the most intense reflections (at  $13^\circ$  and  $27^\circ$ ) correspond to the layered structure of graphite-like carbon nitride. The interplanar spacing is about 3.26 Å, which agrees with the data for materials based on  $\text{g-C}_3\text{N}_4$ . Unfortunately, XRD turned out to be of little use for analysis of deposited metals in such systems: it could only identify metallic platinum with a mass fraction of at least 0.5% (Figure 1A). Iridium compounds could not be identified even at this high mass fraction.

To illustrate how metal concentration affects catalytic activity, two series of catalysts were prepared using Method 1. The series contained Pt with concentration fixed at either 0.5 or 0.1 wt.%, while iridium concentration was varied in rows 0.01, 0.05, 0.1, and 0.5 wt.%. In the case of metal cocatalysts, the actual metal content is a very important factor. Therefore, it was experimentally determined using ICP-AES. The chemical analysis showed that the actual atomic ratios Pt:Ir were in a good linear correlation with the introduced quantities of precursors (Figure S1). The noticeable overconcentration of Pt in the samples can be attributed to the partial decomposition of the  $\text{g-C}_3\text{N}_4$  support during the synthesis. Indeed, the overconcentration correlates with the mass loss previously detected for  $\text{Pt}/\text{g-C}_3\text{N}_4$  materials during their calcination in  $\text{H}_2$  [30].

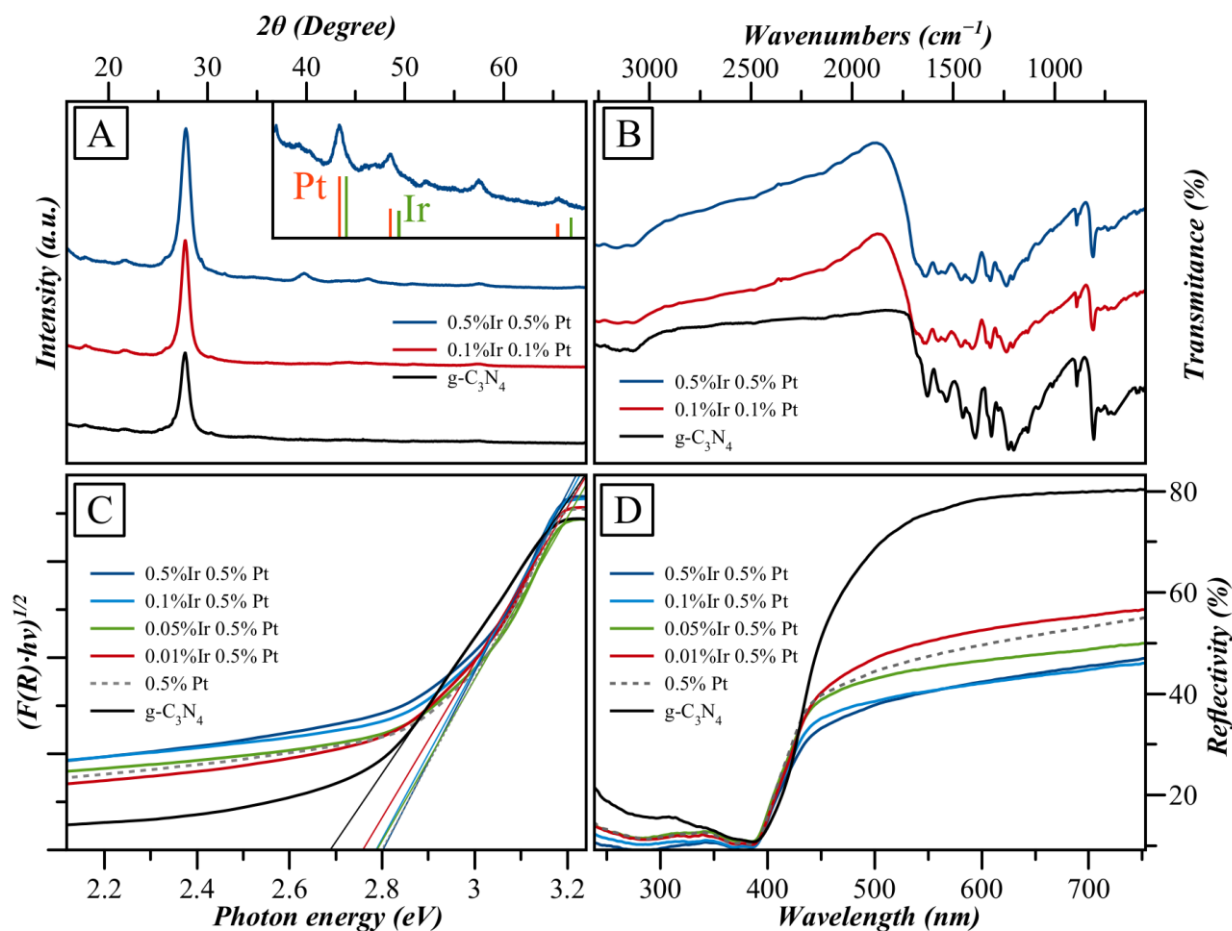


**Figure 1.** (A) XRD patterns of the Pt<sub>0.5</sub>Ir<sub>0.5</sub>/C<sub>3</sub>N<sub>4</sub>(1) and Pt<sub>0.1</sub>Ir<sub>0.1</sub>/C<sub>3</sub>N<sub>4</sub>(1) catalysts and g-C<sub>3</sub>N<sub>4</sub>; (B) FTIR spectra of the Pt<sub>0.5</sub>Ir<sub>0.5</sub>/C<sub>3</sub>N<sub>4</sub>(1), Pt<sub>0.1</sub>Ir<sub>0.1</sub>/C<sub>3</sub>N<sub>4</sub>(1), and g-C<sub>3</sub>N<sub>4</sub>; (C) Tauc plots performed for the Pt<sub>0.5</sub>Ir<sub>y</sub>/C<sub>3</sub>N<sub>4</sub>(1) series of catalysts, Pt<sub>0.5</sub>/C<sub>3</sub>N<sub>4</sub>(1), and g-C<sub>3</sub>N<sub>4</sub>; and (D) DRS of the Pt<sub>0.5</sub>Ir<sub>y</sub>/C<sub>3</sub>N<sub>4</sub>(1) series of catalysts, Pt<sub>0.5</sub>/C<sub>3</sub>N<sub>4</sub>(1) and g-C<sub>3</sub>N<sub>4</sub>.

The FTIR spectra of the materials demonstrate the series of signals in the range 1800–900 cm<sup>-1</sup> which are assigned to the C–N and C–C stretching vibration in agreement with the IR fingerprints of the heptazine-based g-C<sub>3</sub>N<sub>4</sub> materials reported previously [30]. According to the IR spectroscopy data, metal deposition does not lead to any significant changes in the structure of the parent g-C<sub>3</sub>N<sub>4</sub> material (Figure 1B). This result can be ascribed to the low loadings of metals, which makes their influence on the structure of g-C<sub>3</sub>N<sub>4</sub> negligible.

On the other hand, the specific surface area of the samples prepared via Method 1 shows a clear correlation with the amount of Pt: a higher percentage of Pt leads to a higher BET area of a sample. Indeed, the surface area of pristine g-C<sub>3</sub>N<sub>4</sub> is about 50 m<sup>2</sup>·g<sup>-1</sup>, whereas for the samples with 0.1% and 0.5% Pt, the surface area achieves 80 m<sup>2</sup>·g<sup>-1</sup> and 100 m<sup>2</sup>·g<sup>-1</sup>, respectively (Table 1). This result agrees well with our data on monometallic Pt/C<sub>3</sub>N<sub>4</sub> catalysts prepared by reductive (H<sub>2</sub>) thermolysis of PtO<sub>x</sub>/C<sub>3</sub>N<sub>4</sub> precursors [30]. In that case, an increase in the specific surface area was a result of the following process. In a hydrogen atmosphere, Pt nanoparticles serve as catalytic centers for the hydrogenation of the C<sub>3</sub>N<sub>4</sub> framework, resulting in its partial destruction and noticeable porosity growth. Obviously, this process is more pronounced for the samples with higher Pt loadings. The deposition of Pt in the case of Pt-Ir/g-C<sub>3</sub>N<sub>4</sub> catalysts proceeded in the identical manner as for monometallic Pt/g-C<sub>3</sub>N<sub>4</sub>, and therefore the tendency of the BET surface in both cases is similar.

**Table 1.** Textural properties of the Pt-Ir/g-C<sub>3</sub>N<sub>4</sub> catalysts.

Sample (Preparation Method)	S <sub>BET</sub> , m <sup>2</sup> ·g <sup>-1</sup>	V, cm <sup>3</sup> ·g <sup>-1</sup>
g-C <sub>3</sub> N <sub>4</sub>	47.5	0.24
Pt <sub>0.5</sub> Ir <sub>0.1</sub> /C <sub>3</sub> N <sub>4</sub> (1)	97.2	0.37
Pt <sub>0.5</sub> Ir <sub>0.05</sub> /C <sub>3</sub> N <sub>4</sub> (1)	99.3	0.28
Pt <sub>0.5</sub> Ir <sub>0.01</sub> /C <sub>3</sub> N <sub>4</sub> (1)	101	0.36
Pt <sub>0.1</sub> Ir <sub>0.1</sub> /C <sub>3</sub> N <sub>4</sub> (1)	76.8	0.41
Pt <sub>0.1</sub> Ir <sub>0.5</sub> /C <sub>3</sub> N <sub>4</sub> (1)	86.4	0.45
Pt <sub>0.5</sub> Ir <sub>0.5</sub> /C <sub>3</sub> N <sub>4</sub> (2)	120	0.40

In contrast, the fraction of loaded Ir almost does not affect the specific surface area of the samples (Table 1). At the same time, a comparison with the mentioned monometallic Pt/C<sub>3</sub>N<sub>4</sub> catalysts shows that the BET surface of the Pt-Ir/g-C<sub>3</sub>N<sub>4</sub> catalysts is noticeably lower. For example, the surface area of monometallic Pt<sub>0.5</sub>/g-C<sub>3</sub>N<sub>4</sub> achieves 300 m<sup>2</sup>/g, whereas for the bimetallic systems, it does not exceed 120 m<sup>2</sup>/g. This can be due to the partial collapse and blocking of pores after deposition of Ir via impregnation. Note that the highest surface area (120 m<sup>2</sup>·g<sup>-1</sup>) is achieved for the sample Pt<sub>0.5</sub>Ir<sub>0.5</sub>/C<sub>3</sub>N<sub>4</sub>(2), prepared by calcination in hydrogen at the final stage of the synthesis.

The BET surface of Pt-Ir/g-C<sub>3</sub>N<sub>4</sub> catalysts can be particularly enhanced by their calcination in hydrogen after Ir deposition, but (as it has been shown previously and will be clear from the results below) metallic Ir formed in a reductive atmosphere does not possess catalytic activity toward water oxidation.

Diffuse reflectance spectra were obtained for the supported bimetallic photocatalysts with various compositions. Compared to unmodified g-C<sub>3</sub>N<sub>4</sub>, they show a characteristic increase in absorption in the region of 500–700 nm, due to the presence of deposited metal nanoparticles (Figure 1D). This effect is barely visible for catalysts with low metal content but clearly observed for the series Pt<sub>0.5</sub>Ir<sub>y</sub>/C<sub>3</sub>N<sub>4</sub>(1). That said, even for the Pt<sub>0.5</sub>Ir<sub>0.5</sub>/C<sub>3</sub>N<sub>4</sub>(1) catalyst, changes in the position of the band gap are negligible with respect to that for pristine g-C<sub>3</sub>N<sub>4</sub> material, calculated from corresponding Tauc plots (Figure 1C). For bimetallic photocatalysts, the E<sub>g</sub> value varies from 2.75 to 2.80 eV, whereas for pristine g-C<sub>3</sub>N<sub>4</sub> this value amounts to 2.7 eV. This fact agrees with the IR data, and it emphasizes the intactness of the g-C<sub>3</sub>N<sub>4</sub> material after all treatments involved in the preparation of catalysts. In Figure 1D, absorption in the range of 290–400 nm was observed, caused by the surface plasmon resonance effect of platinum and iridium nanoparticles. Most likely, the increase in the energy gap can be associated with the surface plasmon resonance effect inherent in platinum group metals. Previously, the authors [40] also wrote about an increase in the band gap when adding silver nanoparticles.

The surface properties of synthesized Pt-Ir/g-C<sub>3</sub>N<sub>4</sub> photocatalysts were studied by XPS (Figure 2). Peaks corresponding to carbon bonded to nitrogen atoms in the g-C<sub>3</sub>N<sub>4</sub> structure (288.1 eV) were identified in the C1s spectra (Figure S2). The N1s spectrum exhibits four peaks with binding energies at 398.6, 400.0, 401.0, and 404.5 eV (Figure S2). These peaks can be attributed to nitrogen atoms forming, respectively, a CN=C bond, an N-(C)3 bond, an N-H terminal group, and an excited π-bond. The main task was to find the charge state of metals in the bimetallic systems depending on the deposition method. Table 2 shows the surface concentration and oxidation state of the metals, calculated from the XPS data. As seen, the photocatalysts synthesized by Method 1 contain both metals coexisting in the form of metallic (Pt<sup>0</sup>, Ir<sup>0</sup>) and ionic (Pt<sup>2+</sup> and Ir<sup>3+</sup>) species.

The fraction of ionic platinum gradually grows for both series (with 0.1 and 0.5% Pt) with an increase in the iridium loading. This indicates that iridium species additionally promote the oxidation of platinum nanoparticles. For the series with 0.5% Pt, the percentage of metallic platinum varies from 50 to 68%, while for the series with 0.1% Pt, it varies from 24 to 60%. Interestingly, the calcination of the parent monometallic Pt/C<sub>3</sub>N<sub>4</sub> material in air at 400 °C leads to the transformation of only a small part of metallic platinum into the 2+ charge state: in the starting material, there is 95% of Pt<sup>0</sup>, while after calcination in air,

the fraction of Pt<sup>0</sup> decreases to 87% (Figure S3). Therefore, it can be concluded that iridium species can promote the partial oxidation of Pt nanoparticles or isolated Pt atoms.

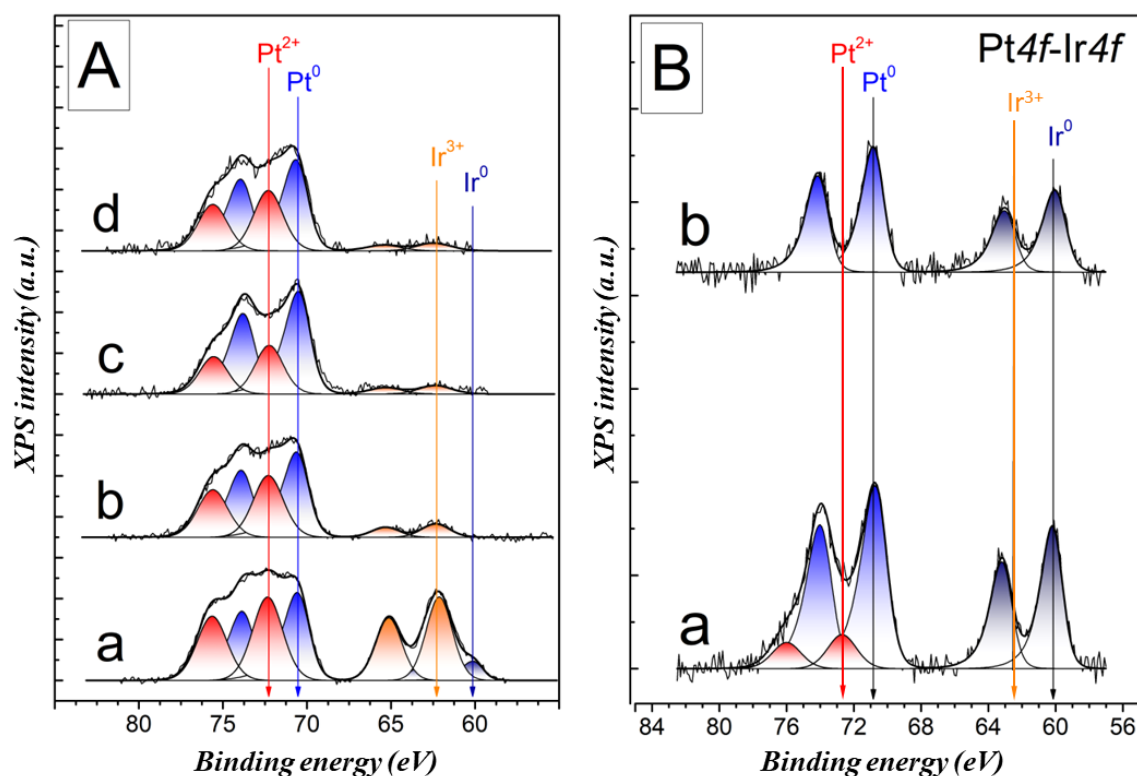


**Figure 2.** (A) Pt4f and Ir4f regions of the XPS spectra of the Pt<sub>0.5</sub>Ir<sub>y</sub>/C<sub>3</sub>N<sub>4</sub>(1) series of catalysts ( $y = 0.5, 0.1, 0.05,$  and  $0.01$  for curves a, b, c, and d correspondingly); and (B) XPS spectra in the same region recorded for the catalysts Pt<sub>0.5</sub>Ir<sub>0.5</sub>/C<sub>3</sub>N<sub>4</sub>(2) (a) and Pt<sub>0.5</sub>Ir<sub>0.5</sub>/C<sub>3</sub>N<sub>4</sub>(3) (b).

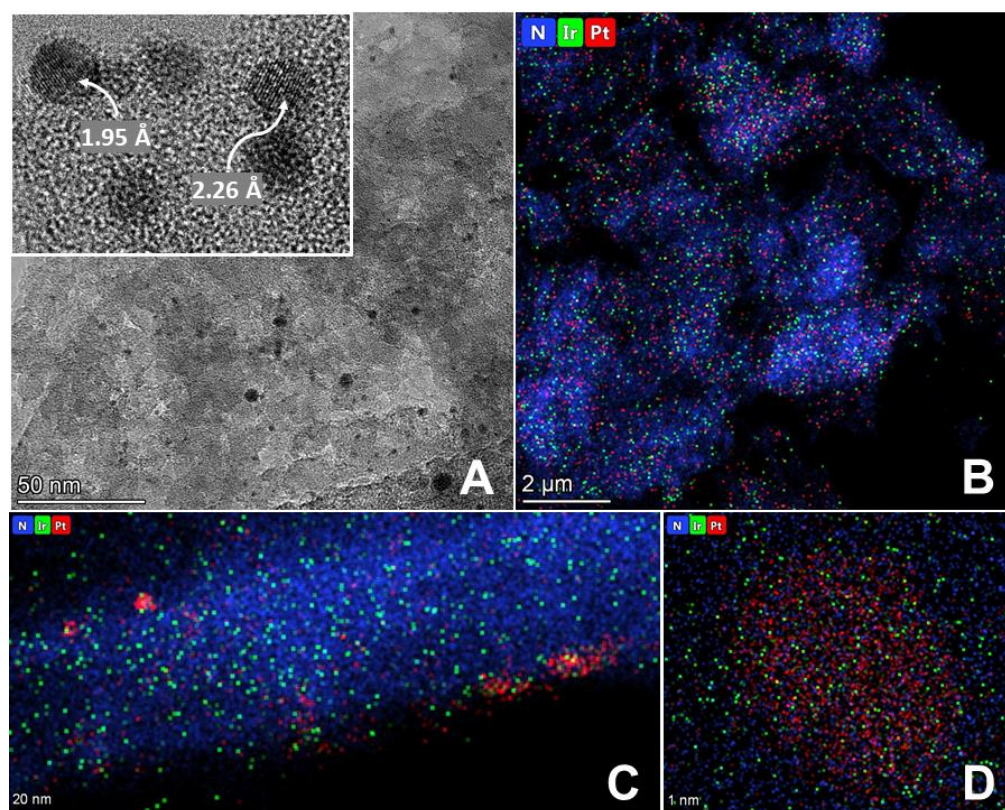
**Table 2.** Ir and Pt concentrations and ratios in the catalyst as found by XPS.

#	Sample	[Pt]/[C]	%, Pt <sup>0</sup>	[Ir]/[C]	%, Ir <sup>0</sup>	[Pt]/[Ir]	[Pt <sup>0</sup> ]/[Ir <sup>3+</sup> ]
Method 1							
1	Pt <sub>0.1</sub> Ir <sub>0.5</sub> /C <sub>3</sub> N <sub>4</sub> (1)	0.0003	24	0.0015	14	0.2	0.06
2	Pt <sub>0.1</sub> Ir <sub>0.1</sub> /C <sub>3</sub> N <sub>4</sub> (1)	0.0004	39	0.0003	13	1.5	0.6
3	Pt <sub>0.1</sub> Ir <sub>0.05</sub> /C <sub>3</sub> N <sub>4</sub> (1)	0.0003	53	0.0002	33	1.8	1.7
4	Pt <sub>0.1</sub> Ir <sub>0.01</sub> /C <sub>3</sub> N <sub>4</sub> (1)	0.0003	60	-	-	-	-
5	Pt <sub>0.5</sub> Ir <sub>0.5</sub> /C <sub>3</sub> N <sub>4</sub> (1)	0.0021	50	0.0012	17	1.7	1.1
6	Pt <sub>0.5</sub> Ir <sub>0.1</sub> /C <sub>3</sub> N <sub>4</sub> (1)	0.0018	57	0.0002	0	10.5	5.9
7	Pt <sub>0.5</sub> Ir <sub>0.05</sub> /C <sub>3</sub> N <sub>4</sub> (1)	0.0018	68	0.0001	0	14.2	9.7
8	Pt <sub>0.5</sub> Ir <sub>0.01</sub> /C <sub>3</sub> N <sub>4</sub> (1)	0.0018	60	-	-	-	-
Method 2							
9	Pt <sub>0.5</sub> Ir <sub>0.5</sub> /C <sub>3</sub> N <sub>4</sub> (2)	0.0006	100	0.0005	100	1.23	-
Method 3							
10	Pt <sub>0.5</sub> Ir <sub>0.5</sub> /C <sub>3</sub> N <sub>4</sub> (3)	0.0011	84	0.0006	100	1.16	-

In all samples prepared by Method 1, iridium is represented mainly by ionic species (Ir<sup>3+</sup>) that can be ascribed to a highly dispersed oxide IrO<sub>x</sub>. It should be noted that for the samples with 0.01 wt.% Ir, the metal is found at the noise level and its oxidation state cannot be identified. For the samples with 0.1% Pt, the surface [Pt]/[Ir] ratio agrees well with its loaded content, whereas in the case of 0.5% Pt, the surface [Pt]/[Ir] content is at least 1.5–2 times higher than the loaded ratio. It can be explained by the effect described earlier—the loss of mass of g-C<sub>3</sub>N<sub>4</sub> during Pt deposition.

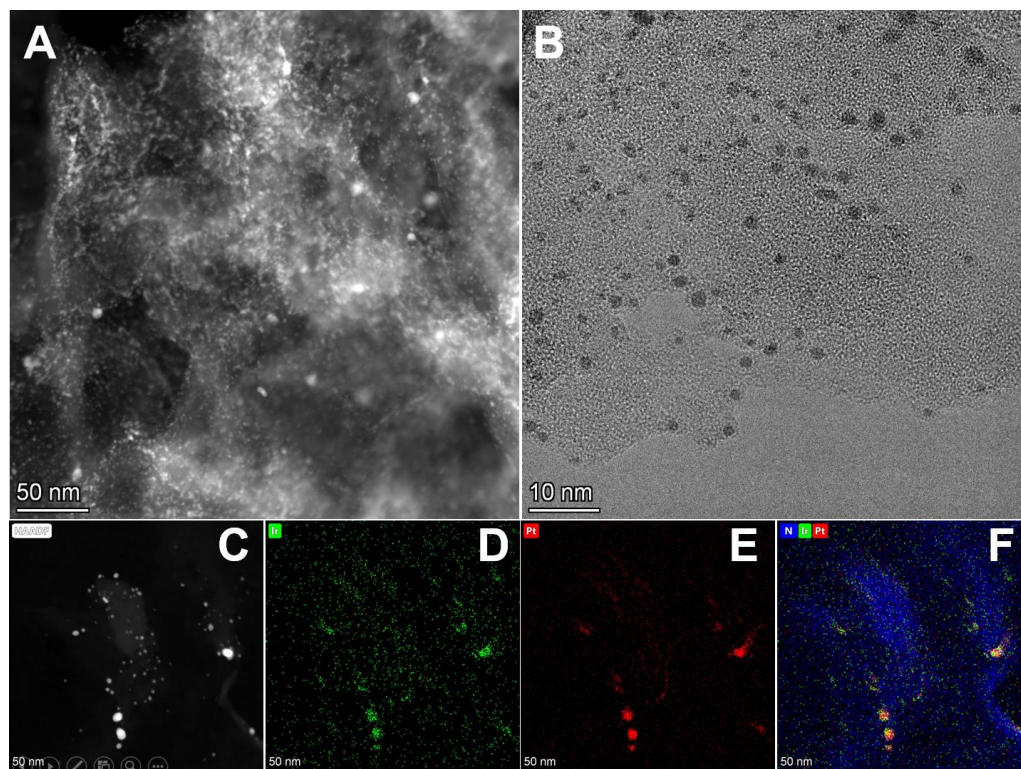
For the sample  $\text{Pt}_{0.5}\text{Ir}_{0.5}/\text{C}_3\text{N}_4(2)$ , prepared by Method 2, which includes the final treatment in hydrogen at 400 °C, both platinum and iridium exist in the metallic state. Under such treatment, the alloying and combined agglomeration of Pt and Ir become more pronounced. For Method 3 (with the “reverse” deposition), the percentage of metallic Pt exceeds 80%, while iridium is reduced to the metallic state completely.

Figure 3 and Figure S4 represent HR-TEM and EDS elemental mapping images of the photocatalyst  $\text{Pt}_{0.5}\text{Ir}_{0.5}/\text{C}_3\text{N}_4(1)$ . The data presented in Figure S4 and Table S1 confirm the presence of C and N elements with the ratio ca. 3:4 in the  $\text{Pt}_{0.5}\text{Ir}_{0.5}/\text{C}_3\text{N}_4(1)$  photocatalyst. The HR-TEM micrographs of the as-prepared catalysts show that platinum tends to aggregate into relatively large nanoparticles on the surface of  $g\text{-C}_3\text{N}_4$ . In contrast, ionic iridium species  $\text{IrO}_x$  are uniformly distributed over the surface of  $g\text{-C}_3\text{N}_4$  and do not form distinct particles. This is consistent with the XRD data revealing that at high metal loadings, the reflexes of Pt become clear, while phases of iridium remain undetectable. On the other hand, the elemental EDS mapping and HR-TEM micrographs (Figure 3B–D) obtained at lower magnification reveal that the overall distribution of both metals over  $g\text{-C}_3\text{N}_4$  particles is quite homogeneous. The interplanar distances (1.95 and 2.26 Å) (Figure 3A and Figure S5) observed for metallic nanoparticles are clearly due to the (200) and (111) indexes of the fcc phase of metallic Pt (1.962 and 2.265 Å distances are reported in the PDF-2 database (card #00-004-0802)) [41]. As seen from Figure S5, isolated (not aggregated) particles show a clear spherical geometry. Due to the proximity of the metallic Pt and Ir cell parameters, it is quite difficult to distinguish their alloys from individual particles. However, even for the  $\text{Ir}_{0.5}\text{Pt}_{0.5}/\text{C}_3\text{N}_4(1)$  sample, the EDS mapping shows that there is no noticeable agglomeration of iridium in the area of the observed metallic nanoparticles compared to the average Ir distribution. Nevertheless, partial alloying of Pt with Ir cannot be excluded.



**Figure 3.** HR-TEM (A) and EDS (B–D) elemental mapping data depicting the metallic nanoparticles observed in the  $\text{Ir}_{0.5}\text{Pt}_{0.5}/g\text{-C}_3\text{N}_4(1)$  photocatalyst.

For comparison, Figure 4 shows TEM images with elemental mapping of the photocatalyst  $\text{Ir}_{0.5}\text{Pt}_{0.5}/\text{g-C}_3\text{N}_4(2)$ , which has the same metal content, but prepared by Method 2. For this sample, elemental mapping shows the formation of large bimetallic Pt-Ir particles up to 10 nm in size. This confirms the alloying of Pt and Ir under hydrogen treatment at 400 °C used in the synthesis by Method 2.



**Figure 4.** (A,C) HAADF, (B) HR-TEM images, and (D–F) EDS elemental mapping representing the metals distribution in  $\text{Ir}_{0.5}\text{Pt}_{0.5}/\text{g-C}_3\text{N}_4(2)$  photocatalyst.

Based on the results above, the following conclusions can be drawn. In the catalysts prepared by Method 1, platinum exists in two states—metallic (up to 60%) and  $\text{Pt}^{2+}$ , while iridium is oxidized predominantly to the  $\text{Ir}^{3+}$  state. However, after Steps 1 and 2 of synthesis, platinum is completely reduced to the metallic state (this was shown earlier for  $\text{Pt}/\text{g-C}_3\text{N}_4$  samples). This means that after Steps 3 and 4, platinum becomes partially oxidized. Moreover, it tends to aggregate into relatively large nanoparticles, while ionic iridium species  $\text{IrO}_x$  are evenly distributed over the surface of  $\text{g-C}_3\text{N}_4$  and do not form distinct particles. In the case of Method 2, with treatment in hydrogen at Step 4, both metals are in the metallic state. In this case, the formation of large alloys of bimetallic Ir-Pt nanoparticles on the surface of  $\text{g-C}_3\text{N}_4$  is observed. For Method 3, with the “reverse” deposition, most of the platinum (over 80%) is in the metallic state, while iridium is reduced to the metallic state completely.

### 2.3. Photocatalytic Tests

The results of kinetic experiments (Table 3) show that the formation of hydrogen from pure water occurs only with the use of the bimetallic photocatalysts prepared by Method 1. In contrast, the photocatalysts  $\text{Pt}_{0.5}\text{Ir}_{0.5}/\text{C}_3\text{N}_4(2)$  and  $\text{Pt}_{0.5}\text{Ir}_{0.5}/\text{C}_3\text{N}_4(3)$ , as well as the reference samples  $\text{Pt}_{0.5}/\text{C}_3\text{N}_4(1)$  and  $\text{Ir}_{0.5}/\text{C}_3\text{N}_4(1)$ , possess zero activity. The activity in hydrogen production from pure water was compared with the activity with the use of a TEOA solution as a substrate. It should be noted that when hydrogen is evolved from aqueous solutions of TEOA, another dependence is observed—for bimetallic photocatalysts  $\text{Pt}_{0.5}\text{Ir}_{0.5}/\text{C}_3\text{N}_4(2)$  and  $\text{Pt}_{0.5}\text{Ir}_{0.5}/\text{C}_3\text{N}_4(3)$ , the activity is much higher than that of the sample

Pt<sub>0.5</sub>Ir<sub>0.5</sub>/C<sub>3</sub>N<sub>4</sub>(1). Indeed, the activity in H<sub>2</sub> evolution from TEOA solutions is higher than for pure water by an order of magnitude.

**Table 3.** Activity of Pt<sub>x</sub>Ir<sub>y</sub>/C<sub>3</sub>N<sub>4</sub> photocatalysts in hydrogen production from ultrapure water and triethanolamine aqueous solution (10 vol.%). Conditions: V<sub>susp</sub> = 50 mL (H<sub>2</sub>O) or 100 mL (TEOA solution), m<sub>cat</sub> = 25 mg, λ<sub>LED</sub> = 400 nm.

#	Method	Metal Loading	Ultrapure H <sub>2</sub> O		10% TEOA Solution		
			W(H <sub>2</sub> ), μmol min <sup>-1</sup>	Activity, μmol H <sub>2</sub> h <sup>-1</sup> g <sub>cat</sub> <sup>-1</sup>	Activity, μmol H <sub>2</sub> O h <sup>-1</sup> g <sub>cat</sub> <sup>-1</sup>	W(H <sub>2</sub> ), μmol min <sup>-1</sup>	Activity, μmol H <sub>2</sub> h <sup>-1</sup> g <sub>cat</sub> <sup>-1</sup>
1		Pt <sub>0.5</sub> /C <sub>3</sub> N <sub>4</sub> (1) *	-	-	-	6.28	7540
2		Pt <sub>0.5</sub> /C <sub>3</sub> N <sub>4</sub> (1)	-	-	-	4.85	5820
3		Ir <sub>0.5</sub> /C <sub>3</sub> N <sub>4</sub> (1)	-	-	-	-	-
4		Pt <sub>0.5</sub> Ir <sub>0.5</sub> /C <sub>3</sub> N <sub>4</sub> (1)	0.023	55.2	29.4	1.06	1270
5		Pt <sub>0.5</sub> Ir <sub>0.1</sub> /C <sub>3</sub> N <sub>4</sub> (1)	0.023	55.2	44.1	0.46	552
6	1	Pt <sub>0.5</sub> Ir <sub>0.05</sub> /C <sub>3</sub> N <sub>4</sub> (1)	0.026	62.4	62.7	0.36	432
7		Pt <sub>0.5</sub> Ir <sub>0.01</sub> /C <sub>3</sub> N <sub>4</sub> (1)	0.043	103	16.8	0.46	552
8		Pt <sub>0.1</sub> Ir <sub>0.5</sub> /C <sub>3</sub> N <sub>4</sub> (1)	0.016	38.4	27.3	0.13	156
9		Pt <sub>0.1</sub> Ir <sub>0.1</sub> /C <sub>3</sub> N <sub>4</sub> (1)	0.019	45.6	35.7	0.06	72
10		Pt <sub>0.1</sub> Ir <sub>0.05</sub> /C <sub>3</sub> N <sub>4</sub> (1)	0.026	62.4	39.9	0.37	444
11		Pt <sub>0.1</sub> Ir <sub>0.01</sub> /C <sub>3</sub> N <sub>4</sub> (1)	0.036	86.4	71.4	0.45	540
12		Pt <sub>0.1</sub> /C <sub>3</sub> N <sub>4</sub> (1)	-	-	-	2.79	3350
13	2	Pt <sub>0.5</sub> Ir <sub>0.5</sub> /C <sub>3</sub> N <sub>4</sub> (2)	-	-	-	7.18	8620
14	3	Pt <sub>0.5</sub> Ir <sub>0.5</sub> /C <sub>3</sub> N <sub>4</sub> (3)	-	-	-	2.74	3290

\* without air treatment at 350 °C.

For comparison, the activity of two monometallic photocatalysts Pt<sub>0.5</sub>/C<sub>3</sub>N<sub>4</sub>(1) was studied. The first of the reference samples was prepared via Steps 1 and 2, while the second one was additionally treated in air at 350 °C, which essentially imitated the preparation of bimetallic samples by Method 1. It was shown that the activity of the first reference photocatalyst (Pt<sub>0.5</sub>/C<sub>3</sub>N<sub>4</sub>(1) \*, 100% Pt in the metallic state) is higher than the activity of the second one (Pt<sub>0.5</sub>/C<sub>3</sub>N<sub>4</sub>(1); 11% Pt in the metallic state and 89% Pt in the Pt<sup>2+</sup> state) in the hydrogen production from an aqueous solution of TEOA, 7.5 and 5.8 mmol h<sup>-1</sup> g<sub>cat</sub><sup>-1</sup>, respectively. In addition, their activity in the production of hydrogen from aqueous solutions of TEOA significantly exceeds the activity of all bimetallic samples prepared by Method 1. Surprisingly, the highest activity in this reaction, 8.6 mmol h<sup>-1</sup> g<sub>cat</sub><sup>-1</sup>, was shown by the bimetallic photocatalyst Pt<sub>0.5</sub>Ir<sub>0.5</sub>/C<sub>3</sub>N<sub>4</sub>(2), in which both platinum and iridium are reduced into the metallic state, which can be explained by the high content of metallic cocatalysts in the necessary oxidation state.

Thus, photocatalysts with platinum in the metallic state exhibit the highest activity in the production of hydrogen from aqueous solutions of an organic electron donor. The transition of platinum to the Pt<sup>2+</sup> state or the deposition of iridium oxides suppresses the photocatalytic activity in this reaction. Regarding the photocatalytic evolution of hydrogen from pure water (without the addition of electron donors), the catalytic effect of platinum is provided by two charge states—Pt<sup>0</sup> and Pt<sup>2+</sup>, but it is necessary that most of the iridium be in the oxidized form.

The next step of the work was to study the effect of the content of iridium and platinum in the samples prepared by Method 1 on the activity in the evolution of hydrogen from pure water. Typical kinetics of hydrogen evolution over bimetallic photocatalysts prepared by Method 1 are shown in Figure 5A,C. The net activities are represented in Table 3 and Figure 5B,D. One can see that the kinetics of hydrogen formation for all the catalysts are linear over 2 h. At that, among photocatalysts Pt<sub>0.5</sub>Ir<sub>y</sub>/C<sub>3</sub>N<sub>4</sub>(1) and Pt<sub>0.1</sub>Ir<sub>y</sub>/C<sub>3</sub>N<sub>4</sub>(1), the maximum rate of hydrogen evolution is about the same, which certainly makes photocatalysts with 0.1% Pt more cost-efficient.

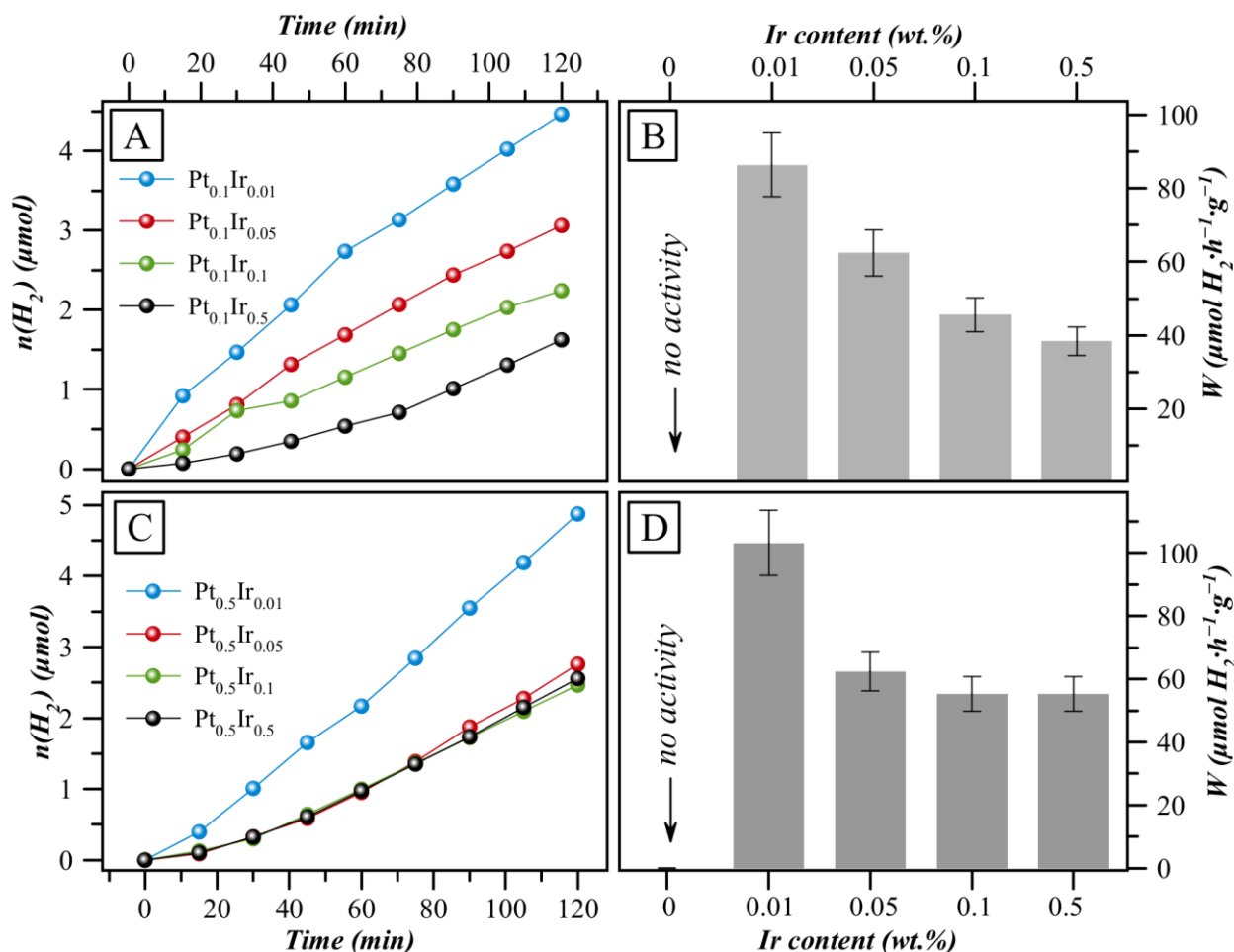


**Figure 5.** (A,C) Kinetic traces for the H<sub>2</sub> generation from ultrapure water by Pt<sub>0.5</sub>Ir<sub>y</sub>/C<sub>3</sub>N<sub>4</sub>(1) and Pt<sub>0.1</sub>Ir<sub>y</sub>/C<sub>3</sub>N<sub>4</sub>(1) photocatalysts ( $y = 0.01, 0.05, 0.1$  and  $0.5$ ) correspondingly under irradiation with 400 nm LED; and (B,D) represent net H<sub>2</sub> evolution rates calculated from the kinetic traces (A,B).

In addition, it is interesting that at a fixed content of platinum, the activity increases with a decrease in the fraction of iridium. Thus, the photocatalysts Pt<sub>0.5</sub>Ir<sub>0.01</sub>/C<sub>3</sub>N<sub>4</sub>(1) and Pt<sub>0.1</sub>Ir<sub>0.01</sub>/C<sub>3</sub>N<sub>4</sub>(1) show the highest activity. In other words, for the splitting of water, it is necessary that platinum content be at least 20 times greater than iridium.

According to our previous results, the rate of hydrogen production in the presence of TEOA over the best 0.5% Pt/g-C<sub>3</sub>N<sub>4</sub> photocatalysts is at the level of 10 mmol h<sup>-1</sup> g<sub>cat</sub><sup>-1</sup>, while the rate of oxygen production from NaIO<sub>4</sub> solutions for 0.5% IrO<sub>x</sub>/g-C<sub>3</sub>N<sub>4</sub> photocatalysts achieves 80 mmol h<sup>-1</sup> g<sub>cat</sub><sup>-1</sup> [30,32]. In addition, as seen from Table 2, the proportion of metallic platinum [Pt<sup>0</sup>]/[Pt] is less than the proportion of oxidized iridium [IrO<sub>x</sub>]/[Ir], i.e., the [Pt<sup>0</sup>]/[Ir<sup>3+</sup>] surface ratio is less than the ratio [Pt]/[Ir]. Accordingly, it can be assumed that iridium oxide catalyzes the formation of oxygen more intensely than metallic platinum catalyzes the formation of hydrogen, which is why active photocatalysts require a large loading of platinum compared to iridium. To the best of our knowledge, this effect has not been published before [6,42].

It should be noted that oxygen was not detected during the reaction, which suggests the presence of other products of water oxidation. It seems most logical that the product of water oxidation is hydrogen peroxide, as has been noted by many researchers [16,20,24,43]. Therefore, we analyzed the reaction product filtrate for the presence of hydrogen peroxide by tests with horseradish peroxidase. Table 3 represents the activities in H<sub>2</sub>O<sub>2</sub> production for Pt<sub>0.5</sub>Ir<sub>y</sub>/C<sub>3</sub>N<sub>4</sub>(1) and Pt<sub>0.1</sub>Ir<sub>y</sub>/C<sub>3</sub>N<sub>4</sub>(1) series. For the Pt<sub>0.1</sub>Ir<sub>y</sub>/C<sub>3</sub>N<sub>4</sub>(1) series, the activity and therefore the amount of evolved H<sub>2</sub>O<sub>2</sub> is at the level of 65–80% of the stoichiometric

amount according to Equation (2). For the samples ranging from  $\text{Pt}_{0.5}\text{Ir}_{0.05}/\text{C}_3\text{N}_4(1)$  to  $\text{Pt}_{0.5}\text{Ir}_{0.5}/\text{C}_3\text{N}_4(1)$ , approximately the same relationship is observed. Only the point on the concentration of hydrogen peroxide for the photocatalyst  $\text{Pt}_{0.5}\text{Ir}_{0.01}/\text{C}_3\text{N}_4(1)$  is an outlier. Incomplete compliance with stoichiometry can be explained by the decomposition of hydrogen peroxide during sample preparation, in particular, the separation of the photocatalyst from the suspension.

An analysis of published data (Table S2 [3,6,8,13,44–47] and Table S3 [18,20,24,48–55]) shows that the obtained activities, ca.  $100 \mu\text{mol h}^{-1} \text{g}_{\text{cat}}^{-1}$ , are among the highest for such systems. For example, a photocatalyst 1% Pt/3% Ir/g- $\text{C}_3\text{N}_4$  shows activity at the same level of  $100 \mu\text{mol h}^{-1} \text{g}_{\text{cat}}^{-1}$ , but at a much higher mass fraction of both noble metals [6]. In general, according to Table S2, for the water splitting with the formation of  $\text{H}_2$  and  $\text{H}_2\text{O}_2$ , photocatalysts based on single-phase g- $\text{C}_3\text{N}_4$  doped with metal cocatalysts are used quite rarely. Moreover, in this case, a discrepancy between the stoichiometry of hydrogen and peroxide is often observed [20,24]. In addition to activity, the stability of photocatalysts is one of the most important aspects. The stability of our photocatalysts was tested in four successive 1.5 h runs of hydrogen production from ultrapure water (Figure 6B). After each run, the reaction suspension was purged with argon to remove gaseous reaction products. One can see that the hydrogen evolution rate remains constant during the runs. The XPS study of the photocatalysts before and after photocatalytic tests (Figure S6) shows that both the surface  $[\text{Pt}]/[\text{C}]$  ratio and the percentage of  $\text{Pt}^0$  also remain almost unchanged. These results are fundamentally different from the data obtained for Pt/g- $\text{C}_3\text{N}_4$  photocatalysts in TEOA solutions, since in that case, the photocatalyst undergoes noticeable deactivation due to the adsorption of oxidation intermediates on its surface [30]. Thus, hydrogen production from pure water seems more promising not only because it is unnecessary to add electron donors but also because of the higher stability of photocatalysts.

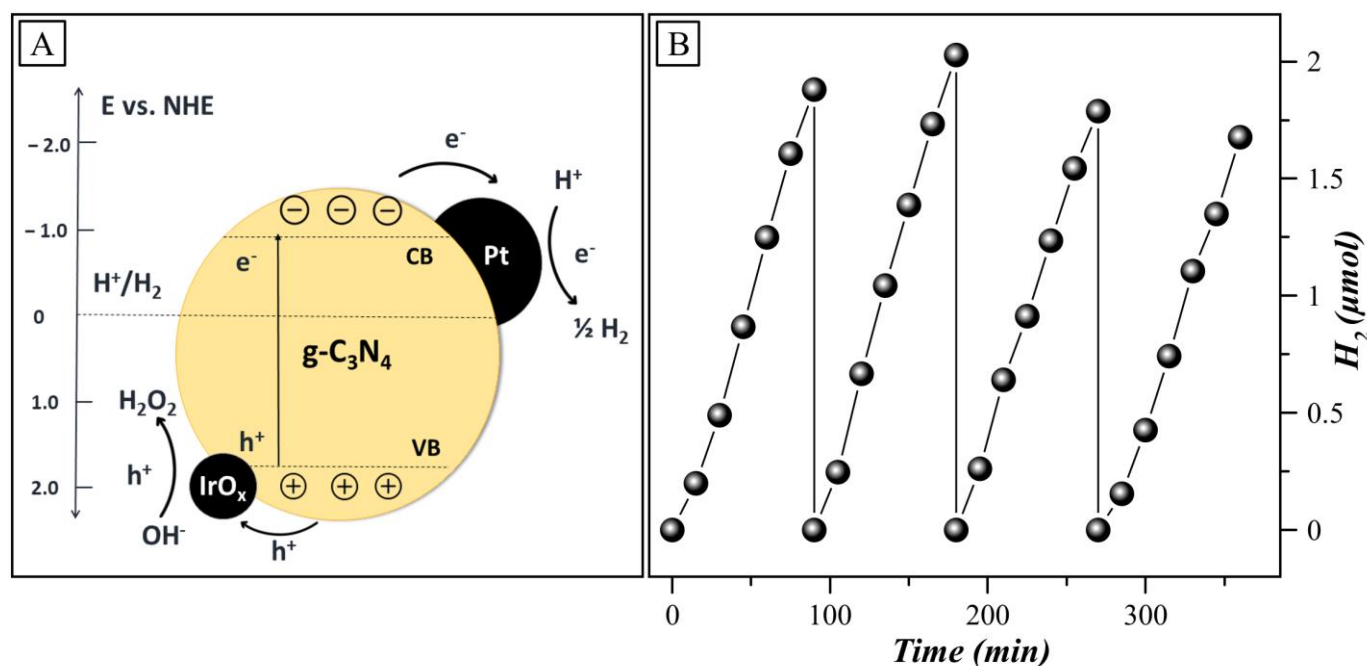


**Figure 6.** (A) Diagram for the proposed mechanism of the  $\text{H}_2$  and  $\text{H}_2\text{O}_2$  generation from water by a visible-light irradiated  $\text{Pt}_x\text{Ir}_y/\text{C}_3\text{N}_4$  photocatalysts; and (B) the cyclic tests of the  $\text{H}_2$  generation from the ultrapure water with the  $\text{Pt}_{0.1}\text{Ir}_y/\text{C}_3\text{N}_4$  photocatalyst.

A probable mechanism of water splitting over a bimetallic photocatalyst is represented in Figure 6A. For efficient water splitting into  $\text{H}_2$  and  $\text{H}_2\text{O}_2$ , the conduction band (CB) level should be more negative than the reduction potential of  $\text{H}^+$  to  $\text{H}_2$  (0 vs. NHE). In addition, the valence band (VB) should be more positive than the oxidation potential of  $\text{H}_2\text{O}$  to  $\text{H}_2\text{O}_2$

(1.78 V) [9,56]. Therefore, g-C<sub>3</sub>N<sub>4</sub>, with the bottom of its CB at -0.8 V and the top of its VB at 1.9 V, meets the requirements for a water splitting photocatalyst [56]. Irradiation at 400 nm excites an electron from the VB of g-C<sub>3</sub>N<sub>4</sub> to its CB. Most likely, photogenerated electrons and holes migrate to particles of metallic platinum and iridium oxide, respectively, where the formation of molecular hydrogen and hydrogen peroxide takes place.

### 3. Materials and Methods

#### 3.1. Starting Reagents and Physical Measurements

All reagents were purchased from commercial suppliers and were used as received. (NH<sub>4</sub>)<sub>3</sub>[Ir(NO<sub>2</sub>)<sub>6</sub>] was synthesized from hydrated iridium trichloride according to the procedure presented in [32]. The obtained (NH<sub>4</sub>)<sub>3</sub>[Ir(NO<sub>2</sub>)<sub>6</sub>] was then characterized by XRD. (Me<sub>4</sub>N)<sub>2</sub>[Pt<sub>2</sub>(μ-OH)<sub>2</sub>(NO<sub>3</sub>)<sub>8</sub>] was obtained from [Pt(H<sub>2</sub>O)<sub>2</sub>(OH)<sub>4</sub>] according to the procedure described in [57]. The purity of (Me<sub>4</sub>N)<sub>2</sub>[Pt<sub>2</sub>(μ-OH)<sub>2</sub>(NO<sub>3</sub>)<sub>8</sub>] was confirmed by XRD and NMR <sup>195</sup>Pt. Graphitic g-C<sub>3</sub>N<sub>4</sub> was obtained by thermal condensation of a supramolecular complex consisting of melamine and cyanuric acid, according to the method presented in [30]. A solution of *fac*-[Ir(H<sub>2</sub>O)<sub>3</sub>(NO<sub>2</sub>)<sub>3</sub>] (0.15M) was prepared from (NH<sub>4</sub>)<sub>3</sub>[Ir(NO<sub>2</sub>)<sub>6</sub>] by its hydrothermal treatment in a 0.3M solution of HNO<sub>3</sub> [32]. Ultrapure water was produced using a Milli-Q system (total org. carbon < 5 ppb (μg/L)).

#### 3.2. Preparation of Pt-Ir/g-C<sub>3</sub>N<sub>4</sub> Catalysts

The catalysts were synthesized using three methods.

Method 1 (Pt-Ir/C<sub>3</sub>N<sub>4</sub>(1)) consisted of the following steps.

1. Deposition of Pt on g-C<sub>3</sub>N<sub>4</sub>. To prepare catalysts with 0.5 or 0.1 wt.% of Pt, an appropriate aliquot (18.0 or 3.60 mL, respectively) of a (Me<sub>4</sub>N)<sub>2</sub>[Pt<sub>2</sub>(μ-OH)<sub>2</sub>(NO<sub>3</sub>)<sub>8</sub>] acetone solution (1.82 mM) was added to a suspension of g-C<sub>3</sub>N<sub>4</sub> (2500 mg) in acetone (40 mL). The resulting suspension was stirred for 12 h at room temperature in a closed vial. The completion of sorption of platinum was checked by the absence of light absorption at 380 nm. The solid was collected by filtration, washed with a copious amount of acetone, and dried in an airflow at room temperature for 20 min.
2. Calcination in H<sub>2</sub>. The resulting material was calcined in hydrogen (400 °C, 10 °C/min ramping, 1 h exposure time) to give a Pt(X)/g-C<sub>3</sub>N<sub>4</sub> precursor. Here, X is the loading of Pt (0.5 or 0.1).
3. Deposition of Ir. The precursor (500.0 mg) was dispersed in 6 mL of acetone, and then an appropriate aliquot (Table 4) of a *fac*-[Ir(H<sub>2</sub>O)<sub>3</sub>(NO<sub>2</sub>)<sub>3</sub>] solution ([Ir] = 4.00 mM) was added. The prepared suspension was thoroughly mixed using ultrasonication (10 min) and then dried in an airflow (200 °C) until complete removal of the solvent.
4. Calcination in air. The obtained powder was calcined in an airflow at 350 °C for 1 h.

**Table 4.** Volumes of *fac*-[Ir(H<sub>2</sub>O)<sub>3</sub>(NO<sub>2</sub>)<sub>3</sub>] solution used for the preparation of catalysts.

Ir wt.% in a Final Catalyst	0.5	0.1	0.05	0.01
V <sub>Ir</sub> (μL)	3266	653	327	65

The resulting materials were designated as Pt<sub>x</sub>Ir<sub>y</sub>/C<sub>3</sub>N<sub>4</sub>(1). Here and below, X and Y are nominal loadings of Pt and Ir, respectively. The actual loadings were determined by ICP-AES.

For comparison reasons, monometallic Pt<sub>x</sub>/C<sub>3</sub>N<sub>4</sub>(1) and Ir<sub>y</sub>/C<sub>3</sub>N<sub>4</sub>(1) catalysts were also synthesized. These materials were prepared from the pristine g-C<sub>3</sub>N<sub>4</sub> using Method 1, excluding Step 3 (for the preparation of Pt<sub>x</sub>/C<sub>3</sub>N<sub>4</sub>(1)) or Steps 1–2 (for the preparation of Ir<sub>y</sub>/C<sub>3</sub>N<sub>4</sub>(1)), respectively.

Method 2 (Pt-Ir/C<sub>3</sub>N<sub>4</sub>(2)). Here, the same protocol was used, except that Step 4 was calcination in a hydrogen flow at 400 °C. The materials obtained by this method were designated as Pt<sub>x</sub>Ir<sub>y</sub>/C<sub>3</sub>N<sub>4</sub>(2).

Method 3 (Pt-Ir/C<sub>3</sub>N<sub>4</sub>(3)). In this protocol, the components were deposited in the reverse order: deposition of Ir on *g*-C<sub>3</sub>N<sub>4</sub>, calcination in air, deposition of Pt, and calcination in H<sub>2</sub>. The materials obtained in this case were designated as Pt<sub>x</sub>Ir<sub>y</sub>/C<sub>3</sub>N<sub>4</sub>(3).

### 3.3. Apparatus

XRD. X-ray powder diffraction analysis of the polycrystalline samples was carried out on a DRON-RM4 diffractometer (Bourestvnik JSC, Saint-Petersburg, Russia, Cu K $\alpha$  radiation, graphite monochromator in the reflected beam, scintillation detector with amplitude discrimination). The samples were prepared by deposition of a suspension in hexane on the polished side of a cell made of fused quartz. A sample of polycrystalline silicon ( $a = 5.4309 \text{ \AA}$ ), prepared similarly, was used as an external standard. The lattice parameters were refined by the full-profile technique using the TOPAS-Academic program, Version 6 [58].

HR-TEM. The structure and microstructure of the photocatalysts were studied by HRTEM using a ThemisZ electron microscope (Thermo Fisher Scientific, Waltham, MA, USA) operated at an accelerating voltage of 200 kV. The microscope was equipped with a corrector of spherical aberrations, which provided a maximum lattice resolution of 0.06 nm, and a SuperX spectrometer (TFS, Plano, TX, USA). Images were recorded using a Ceta 16 CCD sensor (Thermo Fisher Scientific, USA). For electron microscopy studies, samples were deposited on perforated carbon substrates attached to aluminum grids using an ultrasonic dispersant.

UV-vis and DRS. Electron absorbance spectra of the solutions were analyzed with a PG Instruments T60 UV-vis single-beam spectrophotometer. Diffuse reflectance spectroscopy was carried out with a Shimadzu UV-VIS-NIR spectrometer UV-3101 PC (Kyoto, Japan) using BaSO<sub>4</sub> as a reference. The reflectance spectra were recorded in the range of 240–800 nm and presented using the Kubelka–Munk function (K-M).

IR. Infrared spectra were recorded in the range of 400–4000 cm<sup>-1</sup> on a Scimitar FTS 2000 (Varian, Palo Alto, CA, USA) apparatus using tablets of KBr.

XPS. The chemical composition of the samples was studied by the XPS technique on electronic spectrometers SPECS Surface NanoAnalysis GmbH and FLEXPS (Berlin, Germany). The spectrometers were equipped with a hemispherical Phoibos 150 MCD-9 analyzer and Phoibos 150 analyzer with a DLD electron detector, respectively. The spectra were recorded using non-monochromatized AlK $\alpha$  radiation ( $h\nu = 1486.61 \text{ eV}$ ). The background was subtracted from the spectra using the Shirley method [59].

ICP-AES. Elemental analysis was carried out for several samples with the ICP-AES technique with the use of an iCAP-6500 high-resolution spectrometer (Thermo Scientific, Waltham, MA, USA, (ICP-AES)) with a cyclone-type spray chamber and a SeaSpray nebulizer. Samples were dissolved completely in a mixture of sulfuric, nitric, and hydrochloric acid prior to analysis.

### 3.4. Photocatalytic Activity Tests

The synthesized photocatalysts were tested in water splitting. Ordinary distilled water usually contains dissolved organic impurities that can act as electron donors. Therefore, to avoid their influence, we used ultrapure water. The experiments were carried out using a photocatalytic reactor (Figure S7) described in detail elsewhere [32]. First, 25.0 mg of the photocatalyst was suspended in 50 mL of water. After that, the suspension was then purged with argon for 15 min to remove oxygen from the reactor. The reactor was then irradiated with an LED with a wavelength of 400 nm (Figure S7) with parameters (30 V, 1 A; 19 mW·cm<sup>-2</sup>). The hydrogen concentration was recorded on a gas chromatograph “Khromos GC-1000” (manufactured by “Khromos”, Dzerzhinsk, Russia), using a zeolite column and a thermal conductivity detector. Argon was used as a carrier gas. The power density of the LED light source was measured using a ThorLabs Optical Power Monitor (PM16-401).

The amount of hydrogen peroxide formed during the photocatalytic process was measured by UV–vis spectroscopy (UV-250 spectrophotometer (Shimadzu, Kyoto, Japan)) using the reaction of  $\text{H}_2\text{O}_2$  with horseradish peroxidase (HRP) (CAS 9003-99-0, “Diam”, Moscow, Russia) and 3,3',5,5'-tetramethylbenzidine (TMB) (CAS 54827-17-7, NIOPIK, Moscow, Russia) [60]. An acetate–acetic buffer solution with pH 4 was prepared to create the appropriate environment for hydrogen peroxide determination while preventing the overoxidation of TMB. After each water-splitting experiment, a 30 mL aliquot of the suspension was centrifuged for 10 min. The volume of the decanted solution was determined in a measuring cylinder. Subsequently, the solution was transferred to a chemical flask, and 30 mL of buffer solution was added to achieve suitable pH. Additionally, 0.3 mL of a TMB solution in dimethyl sulfoxide (DMSO) and 20  $\mu\text{L}$  of an HRP solution were added. The resulting blue-colored solution was subjected to spectrophotometric analysis using a 1 cm cuvette. The maximum absorption was observed at 652 nm, at which the charge transfer complex, which is formed during partial oxidation with TMB peroxide, has a maximum emission. The concentration of hydrogen peroxide was determined using the Buger–Lambert–Beer equation.

In a separate set of experiments, we studied the activity of synthesized photocatalysts in the production of hydrogen from aqueous solutions of triethanolamine (TEOA, 10 vol.%).

#### 4. Conclusions

Thus, this work proposes a new strategy for the synthesis of bimetallic photocatalysts for water splitting into  $\text{H}_2$  and  $\text{H}_2\text{O}_2$ : the synthesis of Pt/IrO<sub>x</sub>/g-C<sub>3</sub>N<sub>4</sub> photocatalysts with low content of both noble metals. In such systems, platinum acts as a cocatalyst for the reduction of water with the formation of hydrogen, and iridium oxide acts as a cocatalyst for oxidation with the formation of peroxide. A distinctive feature of the proposed synthesis method is the combination of two elements: the preparation of g-C<sub>3</sub>N<sub>4</sub> from melamine cyanurate and the successive deposition of platinum and iridium oxides from their labile complexes. By regulating the order of precursor deposition and the conditions of subsequent thermal treatment, one can directly manage the state of both metals in the resulting materials. From our experiments, we have concluded that the catalytic activity of platinum in the generation of  $\text{H}_2$  is provided by two charge states—Pt<sup>0</sup> and Pt<sup>2+</sup>. However, for the efficient production of  $\text{H}_2\text{O}_2$ , most of the iridium must be oxidized— photocatalysts with iridium in the metallic state are completely inactive in the decomposition of  $\text{H}_2\text{O}$ . To synthesize such materials, platinum was first deposited from a solution of  $(\text{Me}_4\text{N})_2[\text{Pt}_2(\text{OH})_2(\text{NO}_3)_8]$  and then treated with  $\text{H}_2$  at 400 °C. After that, the resulting Pt/C<sub>3</sub>N<sub>4</sub> material was impregnated with an acetone solution of  $([\text{Ir}(\text{H}_2\text{O})_3(\text{NO}_2)_3])$  and calcined in air at 350 °C.

It was found that two tested series of photocatalysts—Pt<sub>0.5</sub>Ir<sub>y</sub>/C<sub>3</sub>N<sub>4</sub> and Pt<sub>0.1</sub>Ir<sub>y</sub>/C<sub>3</sub>N<sub>4</sub>—show approximately the same maximum rate of hydrogen evolution, which certainly makes photocatalysts with 0.1% Pt more promising. At a fixed amount of platinum, the catalyst activity increases with a decrease in the amount of iridium, and for the splitting of water, the platinum content must exceed the iridium content at least 20-fold. The literature data show that the obtained activities ca. 100  $\mu\text{mol h}^{-1} \text{g}_{\text{cat}}^{-1}$  are among the highest achieved for  $\text{H}_2$  production without the use of electron donors over photocatalysts based on g-C<sub>3</sub>N<sub>4</sub>. The proposed synthetic approaches look very promising: they require very low contents of noble metals (0.1 wt.% Pt; 0.01 wt.% Ir), and the “support” they use is available and non-toxic graphite-like carbon nitride without any modifications (doping with non-metals, creating heterostructures, etc.).

**Supplementary Materials:** The following supporting information can be downloaded at: <https://www.mdpi.com/article/10.3390/catal14040225/s1>, Figure S1: Correlation between loaded Ir:Pt ratios and the same value determined with ICP AES chemical analysis in the as-prepared Ir<sub>x</sub>Pt<sub>0.1</sub>/g-C<sub>3</sub>N<sub>4</sub>(1) catalysts (x = 0.5, 0.1, 0.01); Figure S2: C1s and N1s core-level spectra of photocatalysts. The N1s spectra are normalized to the integral intensity of the C1s peaks corresponding to the spectrum of g-C<sub>3</sub>N<sub>4</sub>; Figure S3: XPS spectra of Pt4f of the photocatalysts Pt<sub>0.5</sub>/g-C<sub>3</sub>N<sub>4</sub> after treatment and

hydrogen and consecutive treatment in air. Spectra are normalized to the integral peak intensity C1s corresponding to the carrier spectrum (g-C<sub>3</sub>N<sub>4</sub>); Figure S4: HR-TEM of the Ir<sub>0.5</sub>Pt<sub>0.5</sub>/g-C<sub>3</sub>N<sub>4</sub>(1) photocatalyst, EDS mapping of the C and N elements in the Ir<sub>0.5</sub>Pt<sub>0.5</sub>/g-C<sub>3</sub>N<sub>4</sub>(1) photocatalyst and spectrum from EDS mapping; Figure S5: Analysis of the interplanar distances observed in HR-TEM micrographs of Pt nanoparticles in the Ir<sub>0.5</sub>Pt<sub>0.5</sub>/g-C<sub>3</sub>N<sub>4</sub>(1) photocatalyst; Figure S6: XPS spectra of Pt4f and Ir4f of the spent and fresh Ir<sub>0.01</sub>Pt<sub>0.1</sub>/g-C<sub>3</sub>N<sub>4</sub>(1) photocatalyst. Spectra are normalized to the integral peak intensity C1s corresponding to the carrier spectrum (g-C<sub>3</sub>N<sub>4</sub>); Figure S7: (a) The scheme of photocatalytic reactor utilized in this work and (b) the spectrum of 400 nm LED used for irradiation of catalysts suspensions; Table S1: The percentage composition of all elements calculated from spectrum from EDS mapping; Table S2: Data on the photocatalytic hydrogen and oxygen evolution from water without the addition of electron donors; Table S3: Data on the photocatalytic hydrogen and peroxide evolution from pure water presented in the literature.

**Author Contributions:** N.D.S.: conceptualization, validation, methodology, investigation; P.A.T.: investigation, visualization; A.A.S.: validation, formal analysis, investigation; E.Y.G.: data curation, visualization; A.V.Z.: formal analysis, investigation and data curation; D.B.V.: conceptualization, investigation, visualization and writing—original draft preparation; E.A.K.: conceptualization, visualization, resources, writing—original draft preparation, supervision, project administration, funding acquisition. All authors have read and agreed to the published version of the manuscript.

**Funding:** This work was funded by the Russian Science Foundation (Grant #21-13-00314; <https://rscf.ru/en/project/21-13-00314/>).

**Data Availability Statement:** The data presented in this study are available on request from the corresponding author.

**Acknowledgments:** The TEM and XPS study was carried out using the facility of the shared research center “National center of investigation of catalysts” at Boreskov Institute of Catalysis. The authors deeply thank the XRD Facility of NIIC SB RAS for the FTIR data collection, P.E. Plyusnin for thermogravimetric analysis, and S.V. Cherepanova for XRD analysis.

**Conflicts of Interest:** The authors declare that they have no known competing financial interests or personal relationships that could have appeared to influence the work reported in this paper.

## References

1. Tian, N.; Zhang, Y.; Li, X.; Xiao, K.; Du, X.; Dong, F.; Waterhouse, G.I.N.; Zhang, T.; Huang, H. Precursor-Reforming Protocol to 3D Mesoporous g-C<sub>3</sub>N<sub>4</sub> Established by Ultrathin Self-Doped Nanosheets for Superior Hydrogen Evolution. *Nano Energy* **2017**, *38*, 72–81. [[CrossRef](#)]
2. Zhang, G.; Lan, Z.-A.; Wang, X. Conjugated Polymers: Catalysts for Photocatalytic Hydrogen Evolution. *Angew. Chem. Int. Ed.* **2016**, *55*, 15712–15727. [[CrossRef](#)] [[PubMed](#)]
3. Mo, Z.; Xu, H.; Chen, Z.; She, X.; Song, Y.; Lian, J.; Zhu, X.; Yan, P.; Lei, Y.; Yuan, S.; et al. Construction of MnO<sub>2</sub>/Monolayer g-C<sub>3</sub>N<sub>4</sub> with Mn Vacancies for Z-Scheme Overall Water Splitting. *Appl. Catal. B Environ.* **2019**, *241*, 452–460. [[CrossRef](#)]
4. Zheng, D.; Cao, X.-N.; Wang, X. Precise Formation of a Hollow Carbon Nitride Structure with a Janus Surface to Promote Water Splitting by Photoredox Catalysis. *Angew. Chem. Int. Ed.* **2016**, *55*, 11512–11516. [[CrossRef](#)] [[PubMed](#)]
5. Fujishima, A.; Honda, K. Electrochemical Photolysis of Water at a Semiconductor Electrode One and Two-Dimensional Structure of Alpha-Helix and Beta-Sheet Forms of Poly (L-Alanine) Shown by Specific Heat Measurements at Low Temperatures (1.5–20 K). *Nature* **1972**, *238*, 37–38. [[CrossRef](#)] [[PubMed](#)]
6. Chen, X.; Shi, R.; Chen, Q.; Zhang, Z.; Jiang, W.; Zhu, Y.; Zhang, T. Three-Dimensional Porous g-C<sub>3</sub>N<sub>4</sub> for Highly Efficient Photocatalytic Overall Water Splitting. *Nano Energy* **2019**, *59*, 644–650. [[CrossRef](#)]
7. Navakoteswara Rao, V.; Lakshmana Reddy, N.; Preethi, V.; Karthik, M.; Yu, Y.T.; Yang, J.M.; Mamatha Kumari, M.; Shankar, M.V. A Critical Review on Core/Shell-Based Nanostructured Photocatalysts for Improved Hydrogen Generation. *Int. J. Hydrogen Energy* **2023**, *48*, 11754–11774. [[CrossRef](#)]
8. Liu, Y.; Li, X.; He, H.; Yang, S.; Jia, G.; Liu, S. CoP Imbedded G-C<sub>3</sub>N<sub>4</sub> Heterojunctions for Highly Efficient Photo, Electro and Photoelectrochemical Water Splitting. *J. Colloid Interface Sci.* **2021**, *599*, 23–33. [[CrossRef](#)] [[PubMed](#)]
9. Kozlova, E.A.; Parmon, V.N. Heterogeneous Semiconductor Photocatalysts for Hydrogen Production from Aqueous Solutions of Electron Donors. *Russ. Chem. Rev.* **2017**, *86*, 870–906. [[CrossRef](#)]
10. Bharagav, U.; Ramesh Reddy, N.; Nava Koteswara Rao, V.; Ravi, P.; Sathish, M.; Rangappa, D.; Prathap, K.; Shilpa Chakra, C.; Shankar, M.V.; Appels, L.; et al. Bifunctional G-C<sub>3</sub>N<sub>4</sub>/Carbon Nanotubes/WO<sub>3</sub> Ternary Nanohybrids for Photocatalytic Energy and Environmental Applications. *Chemosphere* **2023**, *311*, 137030. [[CrossRef](#)]
11. Hainer, A.S.; Hodgins, J.S.; Sandre, V.; Vallieres, M.; Lanterna, A.E.; Scaiano, J.C. Photocatalytic Hydrogen Generation Using Metal-Decorated TiO<sub>2</sub>: Sacrificial Donors vs. True Water Splitting. *ACS Energy Lett.* **2018**, *3*, 542–545. [[CrossRef](#)]

12. Solakidou, M.; Giannakas, A.; Georgiou, Y.; Boukos, N.; Louloudi, M.; Deligiannakis, Y. Efficient Photocatalytic Water-Splitting Performance by Ternary CdS/Pt-N-TiO<sub>2</sub> and CdS/Pt-N,F-TiO<sub>2</sub>: Interplay between CdS Photo Corrosion and TiO<sub>2</sub>-Dopping. *Appl. Catal. B Environ.* **2019**, *254*, 194–205. [[CrossRef](#)]
13. He, H.; Cao, J.; Guo, M.; Lin, H.; Zhang, J.; Chen, Y.; Chen, S. Distinctive Ternary CdS/Ni<sub>2</sub>P/g-C<sub>3</sub>N<sub>4</sub> Composite for Overall Water Splitting: Ni<sub>2</sub>P Accelerating Separation of Photocarriers. *Appl. Catal. B Environ.* **2019**, *249*, 246–256. [[CrossRef](#)]
14. Yan, J.; Wu, H.; Chen, H.; Zhang, Y.; Zhang, F.; Liu, S.F. Fabrication of TiO<sub>2</sub>/C<sub>3</sub>N<sub>4</sub> Heterostructure for Enhanced Photocatalytic Z-Scheme Overall Water Splitting. *Appl. Catal. B Environ.* **2016**, *191*, 130–137. [[CrossRef](#)]
15. Yu, J.; Wu, S.; Zhao, X.; Li, Z.; Yang, X.; Shen, Q.; Lu, M.; Xie, X.; Zhan, D.; Yan, J. Progress on Two-Dimensional Transitional Metal Dichalcogenides Alloy Materials: Growth, Characterisation, and Optoelectronic Applications. *Nanomaterials* **2023**, *13*, 2843. [[CrossRef](#)] [[PubMed](#)]
16. Xue, F.; Si, Y.; Wang, M.; Liu, M.; Guo, L. Toward Efficient Photocatalytic Pure Water Splitting for Simultaneous H<sub>2</sub> and H<sub>2</sub>O<sub>2</sub> Production. *Nano Energy* **2019**, *62*, 823–831. [[CrossRef](#)]
17. Wang, Z.; Inoue, Y.; Hisatomi, T.; Ishikawa, R.; Wang, Q.; Takata, T.; Chen, S.; Shibata, N.; Ikuhara, Y.; Domen, K. Overall Water Splitting by Ta<sub>3</sub>N<sub>5</sub> Nanorod Single Crystals Grown on the Edges of KTaO<sub>3</sub> Particles. *Nat. Catal.* **2018**, *1*, 756–763. [[CrossRef](#)]
18. Zhu, M.; Zhu, C.; Wu, D.; Wang, X.; Wang, H.; Gao, J.; Huang, H.; Shi, C.; Liu, Y.; Kang, Z. Efficient Photocatalytic Water Splitting through Titanium Silicalite Stabilized CoO Nanodots. *Nanoscale* **2019**, *11*, 15984–15990. [[CrossRef](#)]
19. Xiang, Q.; Yu, J.; Jaroniec, M. Preparation and Enhanced Visible-Light Photocatalytic H<sub>2</sub>-Production Activity of Graphene/C<sub>3</sub>N<sub>4</sub> Composites. *J. Phys. Chem. C* **2011**, *115*, 7355–7363. [[CrossRef](#)]
20. Hu, S.; Sun, X.; Zhao, Y.; Li, W.; Wang, H.; Wu, G. The Effective Photocatalytic Water Splitting to Simultaneously Produce H<sub>2</sub> and H<sub>2</sub>O<sub>2</sub> over Pt Loaded K-g-C<sub>3</sub>N<sub>4</sub> Catalyst. *J. Taiwan Inst. Chem. Eng.* **2020**, *107*, 129–138. [[CrossRef](#)]
21. Lu, W.; Yi, Z.; Zhang, J.; Xu, X.; Tang, B.; Li, G.; Zeng, L.; Chen, J.; Sun, T. A Tunable Broadband Absorber in the Terahertz Band Based on the Proportional Structure of a Single Layer of Graphene. *Diam. Relat. Mater.* **2023**, *140*, 110481. [[CrossRef](#)]
22. Zhou, S.; Bi, K.; Li, Q.; Mei, L.; Niu, Y.; Fu, W.; Han, S.; Zhang, S.; Mu, J.; Tan, L.; et al. Patterned Graphene-Based Metamaterials for Terahertz Wave Absorption. *Coatings* **2023**, *13*, 59. [[CrossRef](#)]
23. Lai, R.; Chen, H.; Zhou, Z.; Yi, Z.; Tang, B.; Chen, J.; Yi, Y.; Tang, C.; Zhang, J.; Sun, T. Design of a Penta-Band Graphene-Based Terahertz Metamaterial Absorber with Fine Sensing Performance. *Micromachines* **2023**, *14*, 1802. [[CrossRef](#)] [[PubMed](#)]
24. Liang, F.; Sun, X.; Hu, S.; Ma, H.; Wang, F.; Wu, G. Photocatalytic Water Splitting to Simultaneously Produce H<sub>2</sub> and H<sub>2</sub>O<sub>2</sub> by Two-Electron Reduction Process over Pt Loaded Na<sup>+</sup> Introduced g-C<sub>3</sub>N<sub>4</sub> Catalyst. *Diam. Relat. Mater.* **2020**, *108*, 107971. [[CrossRef](#)]
25. Wang, X.; Maeda, K.; Thomas, A.; Takanabe, K.; Xin, G.; Carlsson, J.M.; Domen, K.; Antonietti, M. A Metal-Free Polymeric Photocatalyst for Hydrogen Production from Water under Visible Light. *Nat. Mater.* **2009**, *8*, 76–80. [[CrossRef](#)] [[PubMed](#)]
26. Ye, S.; Wang, R.; Wu, M.-Z.; Yuan, Y.-P. A Review on G-C<sub>3</sub>N<sub>4</sub> for Photocatalytic Water Splitting and CO<sub>2</sub> Reduction. *Appl. Surf. Sci.* **2015**, *358*, 15–27. [[CrossRef](#)]
27. Liu, J.; Liu, Y.; Liu, N.; Han, Y.; Zhang, X.; Huang, H.; Lifshitz, Y.; Lee, S.-T.; Zhong, J.; Kang, Z. Metal-Free Efficient Photocatalyst for Stable Visible Water Splitting via a Two-Electron Pathway. *Science* **2015**, *347*, 970–974. [[CrossRef](#)] [[PubMed](#)]
28. Wu, X.; Zhu, C.; Wang, L.; Guo, S.; Zhang, Y.; Li, H.; Huang, H.; Liu, Y.; Tang, J.; Kang, Z. Control Strategy on Two-/Four-Electron Pathway of Water Splitting by Multidoped Carbon Based Catalysts. *ACS Catal.* **2017**, *7*, 1637–1645. [[CrossRef](#)]
29. Zhurenok, A.V.; Vasilchenko, D.B.; Kozlova, E.A. Comprehensive Review on G-C<sub>3</sub>N<sub>4</sub>-Based Photocatalysts for the Photocatalytic Hydrogen Production under Visible Light. *Int. J. Mol. Sci.* **2023**, *24*, 346. [[CrossRef](#)]
30. Vasilchenko, D.; Zhurenok, A.; Saraev, A.; Gerasimov, E.; Cherepanova, S.; Tkachev, S.; Plusnin, P.; Kozlova, E. Highly Efficient Hydrogen Production under Visible Light over G-C<sub>3</sub>N<sub>4</sub>-Based Photocatalysts with Low Platinum Content. *Chem. Eng. J.* **2022**, *445*, 136721. [[CrossRef](#)]
31. Vasilchenko, D.; Tkachenko, P.; Tkachev, S.; Popovetskiy, P.; Komarov, V.; Asanova, T.; Asanov, I.; Filatov, E.; Maximovskiy, E.; Gerasimov, E.; et al. Sulfuric Acid Solutions of [Pt(OH)<sub>4</sub>(H<sub>2</sub>O)<sub>2</sub>]: A Platinum Speciation Survey and Hydrated Pt(IV) Oxide Formation for Practical Use. *Inorg. Chem.* **2022**, *61*, 9667–9684. [[CrossRef](#)] [[PubMed](#)]
32. Topchiyan, P.; Vasilchenko, D.; Tkachev, S.; Sheven, D.; Eltsov, I.; Asanov, I.; Sidorenko, N.; Saraev, A.; Gerasimov, E.; Kurenkova, A.; et al. Highly Active Visible Light-Promoted Ir/g-C<sub>3</sub>N<sub>4</sub> Photocatalysts for the Water Oxidation Reaction Prepared from a Halogen-Free Iridium Precursor. *ACS Appl. Mater. Interfaces* **2022**, *14*, 35600–35612. [[CrossRef](#)] [[PubMed](#)]
33. Li, R.; Li, C. Photocatalytic Water Splitting on Semiconductor-Based Photocatalysts. *Adv. Catal.* **2017**, *60*, 1–57. [[CrossRef](#)]
34. Wang, Z.; Li, C.; Domen, K. Recent Developments in Heterogeneous Photocatalysts for Solar-Driven Overall Water Splitting. *Chem. Soc. Rev.* **2019**, *48*, 2109–2125. [[CrossRef](#)] [[PubMed](#)]
35. Maheskumar, V.; Saravanakumar, K.; Yea, Y.; Yoon, Y.; Park, C.M. Construction of Heterostructure Interface with FeNi<sub>2</sub>S<sub>4</sub> and CoFe Nanowires as an Efficient Bifunctional Electrocatalyst for Overall Water Splitting and Urea Electrolysis. *Int. J. Hydrog. Energy* **2023**, *48*, 5080–5094. [[CrossRef](#)]
36. Maheskumar, V.; Saravanakumar, K.; Govindan, J.; Park, C.M. Rational Design of Double Perovskite La<sub>2</sub>Ni<sub>0.5</sub>Co<sub>0.5</sub>MnO<sub>6</sub> Decorated Polyaniline Array on MoO<sub>3</sub> Nanobelts with Strong Heterointerface Boosting Oxygen Evolution Reaction and Urea Oxidation. *Appl. Surf. Sci.* **2023**, *612*, 155737. [[CrossRef](#)]
37. Pan, Z.; Zheng, Y.; Guo, F.; Niu, P.; Wang, X. Decorating CoP and Pt Nanoparticles on Graphitic Carbon Nitride Nanosheets to Promote Overall Water Splitting by Conjugated Polymers. *ChemSusChem* **2017**, *10*, 87–90. [[CrossRef](#)] [[PubMed](#)]

38. Zhang, G.; Lan, Z.-A.; Lin, L.; Lin, S.; Wang, X. Overall Water Splitting by Pt/g-C<sub>3</sub>N<sub>4</sub> Photocatalysts without Using Sacrificial Agents. *Chem. Sci.* **2016**, *7*, 3062–3066. [[CrossRef](#)]
39. Pan, Z.; Wang, S.; Niu, P.; Liu, M.; Wang, X. Photocatalytic Overall Water Splitting by Spatially-Separated Rh and RhOx Cocatalysts on Polymeric Carbon Nitride Nanosheets. *J. Catal.* **2019**, *379*, 129–137. [[CrossRef](#)]
40. Mosiori, C.O.; Njoroge, W.K.; Ochoo, L.O. Optical Analysis of Ag-NPs Containing Methyl Ammonium Lead Tri-Iodide Thin Films. *Path Sci.* **2017**, *3*, 2007–2015. [[CrossRef](#)]
41. Navakoteswara Rao, V.; Ravi, P.; Sathish, M.; Cheralathan, K.K.; Neppolian, B.; Mamatha Kumari, M.; Shankar, M.V. Manifestation of Enhanced and Durable Photocatalytic H<sub>2</sub> Production Using Hierarchically Structured Pt@Co<sub>3</sub>O<sub>4</sub>/TiO<sub>2</sub> Ternary Nanocomposite. *Ceram. Int.* **2021**, *47*, 10226–10235. [[CrossRef](#)]
42. Moon, H.S.; Hsiao, K.; Wu, M.; Yun, Y.; Hsu, Y.; Yong, K. Spatial Separation of Cocatalysts on Z-Scheme Organic/Inorganic Heterostructure Hollow Spheres for Enhanced Photocatalytic H<sub>2</sub> Evolution and In-Depth Analysis of the Charge-Transfer Mechanism. *Adv. Mater.* **2023**, *35*, 2200172. [[CrossRef](#)]
43. Li, Z.; Kong, C.; Lu, G. Visible Photocatalytic Water Splitting and Photocatalytic Two-Electron Oxygen Formation over Cu- and Fe-Doped g-C<sub>3</sub>N<sub>4</sub>. *J. Phys. Chem. C* **2016**, *120*, 56–63. [[CrossRef](#)]
44. Xie, H.; Zhao, Y.; Li, H.; Xu, Y.; Chen, X. 2D BiVO<sub>4</sub>/g-C<sub>3</sub>N<sub>4</sub> Z-Scheme Photocatalyst for Enhanced Overall Water Splitting. *J. Mater. Sci.* **2019**, *54*, 10836–10845. [[CrossRef](#)]
45. Dai, D.; Wang, P.; Bao, X.; Xu, Y.; Wang, Z.; Guo, Y.H.; Wang, Z.; Zheng, Z.; Liu, Y.; Cheng, H.; et al. G-C<sub>3</sub>N<sub>4</sub>/ITO/Co-BiVO<sub>4</sub> Z-Scheme Composite for Solar Overall Water Splitting. *Chem. Eng. J.* **2022**, *433*, 134476. [[CrossRef](#)]
46. Xu, B.B.; Fu, X.B.; You, X.M.; Zhao, E.; Li, F.F.; Chen, Z.; Li, Y.X.; Wang, X.L.; Yao, Y.F. Synergistic Promotion of Single-Atom Co Surrounding a PtCo Alloy Based on a g-C<sub>3</sub>N<sub>4</sub> Nanosheet for Overall Water Splitting. *ACS Catal.* **2022**, *12*, 6958–6967. [[CrossRef](#)]
47. Gong, Q.; Zhou, Y.; Wang, R.; Jiao, W. Enhanced Photocatalytic Pure Water Splitting of Porous G-C<sub>3</sub>N<sub>4</sub>/CdS Composite by the Bimetallic Phosphide. *J. Environ. Chem. Eng.* **2022**, *10*, 108046. [[CrossRef](#)]
48. Xue, F.; Si, Y.; Cheng, C.; Fu, W.; Chen, X.; Shen, S.; Wang, L.; Liu, M. Electron Transfer via Homogeneous Phosphorus Bridges Enabling Boosted Photocatalytic Generation of H<sub>2</sub> and H<sub>2</sub>O<sub>2</sub> from Pure Water with Stoichiometric Ratio. *Nano Energy* **2022**, *103*, 107799. [[CrossRef](#)]
49. Liu, Y.; Zhao, Y.; Wu, Q.; Wang, X.; Nie, H.; Zhou, Y.; Huang, H.; Shao, M.; Liu, Y.; Kang, Z. Charge Storage of Carbon Dot Enhances Photo-Production of H<sub>2</sub> and H<sub>2</sub>O<sub>2</sub> over Ni<sub>2</sub>P/Carbon Dot Catalyst under Normal Pressure. *Chem. Eng. J.* **2021**, *409*, 128184. [[CrossRef](#)]
50. Ai, Z.; Zhang, K.; Xu, L.; Huang, M.; Shi, D.; Shao, Y.; Shen, J.; Wu, Y.; Hao, X. In Situ Configuration of Dual S-Scheme BP/(Ti<sub>3</sub>C<sub>2</sub>Tx@TiO<sub>2</sub>) Heterojunction for Broadband Spectrum Solar-Driven Photocatalytic H<sub>2</sub> Evolution in Pure Water. *J. Colloid Interface Sci.* **2022**, *610*, 13–23. [[CrossRef](#)]
51. Zhang, L.; Dong, W.; Zhang, Y.; Song, X.; Jiang, H. Precisely Anchoring Ni-Doped Cobalt Phosphide Nanoparticles on Phosphatized Carbon Nitride for Efficient Photocatalytic Water Splitting. *Chem. Eng. J.* **2023**, *472*, 144898. [[CrossRef](#)]
52. Liu, Y.; Zhao, Y.; Sun, Y.; Cao, J.; Wang, H.; Wang, X.; Huang, H.; Shao, M.; Liu, Y.; Kang, Z. A 4e<sup>-</sup>-2e<sup>-</sup> Cascaded Pathway for Highly Efficient Production of H<sub>2</sub> and H<sub>2</sub>O<sub>2</sub> from Water Photo-Splitting at Normal Pressure. *Appl. Catal. B Environ.* **2020**, *270*, 118875. [[CrossRef](#)]
53. Dou, Y.; Zhu, C.; Zhu, M.; Fu, Y.; Wang, H.; Shi, C.; Huang, H.; Liu, Y.; Kang, Z. Highly Mesoporous Carbon Nitride Photocatalysts for Efficient and Stable Overall Water Splitting. *Appl. Surf. Sci.* **2020**, *509*, 144706. [[CrossRef](#)]
54. Zhang, E.; Zhu, Q.; Huang, J.; Liu, J.; Tan, G.; Sun, C.; Li, T.; Liu, S.; Li, Y.; Wang, H.; et al. Visually Resolving the Direct Z-Scheme Heterojunction in CdS@ZnIn<sub>2</sub>S<sub>4</sub> Hollow Cubes for Photocatalytic Evolution of H<sub>2</sub> and H<sub>2</sub>O<sub>2</sub> from Pure Water. *Appl. Catal. B Environ.* **2021**, *293*, 120213. [[CrossRef](#)]
55. Fang, W.L.; Wang, L.; Li, C.H. Preparation of Au-OVs-BiOBr-P25 Z-Scheme Photocatalyst and Its Photocatalytic Performance in Overall Water Splitting. *Ranliao Huaxue Xuebao/J. Fuel Chem. Technol.* **2022**, *50*, 446–455. [[CrossRef](#)]
56. Cao, J.; Wang, H.; Zhao, Y.; Liu, Y.; Wu, Q.; Huang, H.; Shao, M.; Liu, Y.; Kang, Z. Phosphorus-Doped Porous Carbon Nitride for Efficient Sole Production of Hydrogen Peroxide via Photocatalytic Water Splitting with a Two-Channel Pathway. *J. Mater. Chem. A* **2020**, *8*, 3701–3707. [[CrossRef](#)]
57. Vasilchenko, D.; Topchiyan, P.; Berdyugin, S.; Filatov, E.; Tkachev, S.; Baidina, I.; Komarov, V.; Slavinskaya, E.; Stadnichenko, A.; Gerasimov, E. Tetraalkylammonium Salts of Platinum Nitrate Complexes: Isolation, Structure, and Relevance to the Preparation of PtOx/CeO<sub>2</sub> Catalysts for Low-Temperature CO Oxidation. *Inorg. Chem* **2019**, *58*, 6075–6087. [[CrossRef](#)] [[PubMed](#)]
58. Coelho, A.A. *TOPAS-Academic, Version 6 (Computer Software)*; Coelho Software: Brisbane, Australia, 2007.
59. Shirley, D.A. High-Resolution X-ray Photoemission Spectrum of the Valence Bands of Gold. *Phys. Rev. B* **1972**, *5*, 4709–4714. [[CrossRef](#)]
60. Bally, R.W.; Gribnau, T.C.J. Some Aspects of the Chromogen 3,3',5,5'-Tetramethylbenzidine as Hydrogen Donor in a Horseradish Peroxidase Assay. *Clin. Chem. Lab. Med.* **1989**, *27*, 791–796. [[CrossRef](#)]

**Disclaimer/Publisher's Note:** The statements, opinions and data contained in all publications are solely those of the individual author(s) and contributor(s) and not of MDPI and/or the editor(s). MDPI and/or the editor(s) disclaim responsibility for any injury to people or property resulting from any ideas, methods, instructions or products referred to in the content.